Fault slip analysis in the Koralm Massif (Eastern Alps) and consequences for the final uplift of "cold spots" in Miocene times

GERALD PISCHINGER[1], WALTER KURZ[2,*], MARTIN ÜBLEIS[1], MAGDALENA EGGER[1], HARALD FRITZ[2], FRANZ JOSEF BROSCH[1] & KARL STINGL[3]

ABSTRACT

The Paleogene and Neogene evolution of Austroalpine basement units east of the Tauern Window is characterised by the formation of two major sets of faults: (1) ESE–WNW- to E–W-trending faults, associated with ENE- and NNW-trending conjugate structures and (2) N–S to NNE-SSW striking structures, mainly acting as high-angle normal faults, often associated with E-dipping low-angle normal faults along the western margin of the Styrian Basin.

Together with the stratigraphic evolution of the Styrian and Lavanttal Basins and the related subsidence histories a tectonic evolution may be reconstructed for this part of the Eastern Alps. In the southern part of the Koralm Massif, WNW-trending fractures were activated as dextral strike-slip faults, associated with the evolution of WNW-trending troughs filled up with coarse block debris. W- to WNW-trending fractures were reactivated as normal faults, indicating N–S extension. It is assumed that these phases resulted in subsid-

ence and block debris sedimentation in Karpatian and Badenian times (ca. 17–13 Ma).

In the Western Styrian Basin no Sarmatian (13–11.5 Ma) sediments are observed; Pannonian (11.5 to 7.1 Ma) sediments are restricted to the Eastern Styrian Basin. This indicates, that the Koralm basement and the Western Styrian Basin were affected by post-Sarmatian uplift, coinciding with a re-activation of N-trending normal faults along the eastern margin of the Koralm Massif. Therefore, we suggest that the final uplift of the Koralm Complex, partly together with the Western Styrian Basin, occurred during the early Pannonian (at approximately 10 Ma). The elevation of clastic deposits indicates that the Koralm Complex was elevated by approximately 800 m during this phase, associated with an additional phase of E–W-directed extension accommodated by N–S striking normal faults.

---

1 Introduction

In contrast to its structural evolution during the Cretaceous period, little is known about the Paleogene and Neogene evolution of the Koralm Complex (Figs. 1, 2), even though late-orogenic strike-slip and extensional faulting that occurred during the Miocene (e.g. Ratschbacher et al. 1991) are well-known on a regional scale and brought about the final shaping of the orogen (e.g. Frisch et al. 1998). It is widely assumed that the formation of the Lavanttal fault system is related to this tectonic scenario as well (e.g. Frisch et al. 1998, 2000a, b; Reinecker 2000). Although large-scale models providing the reconstruction of the structural evolution of the central and eastern parts of the Eastern Alps (Fig. 1) during the Cenozoic and in particular the Neogene exist (e.g. Neubauer & Genser 1990; Decker & Peresson 1996; Peresson & Decker 1997; Neubauer et al. 2000), a model for the final exhumation of the Koralm Complex has not

been established yet. To a great extent this may be related to the restricted access to well preserved exposures in this area.

In this study we discuss the final evolution of this unit during the Miocene by the analysis of faults, fault zones and related structures, and the relationships to and the time constraints given by the adjacent sedimentary basins. Particular emphasis will be placed on the southeastern part of the Koralm Massif and the adjacent parts of the Styrian Basin. This area is characterised by the occurrence of coarse, blocky debris deposits (the so-called "Schwanberg Blockschutt") (Flügel & Neubauer 1984), or Schwanberg Formation (Nebert 1989) along an E–W trending basin. This sedimentary trough encroaches the Koralm Massif towards west (Fig. 2). Compared with the Neogene deposits of the western Styrian Basin, both the base and the top of the "Schwanberg Blockschutt" trough are at a higher altitude. Therefore, the analysis of the mechanisms of its inversion and elevation relative to the main Styrian Basin will provide
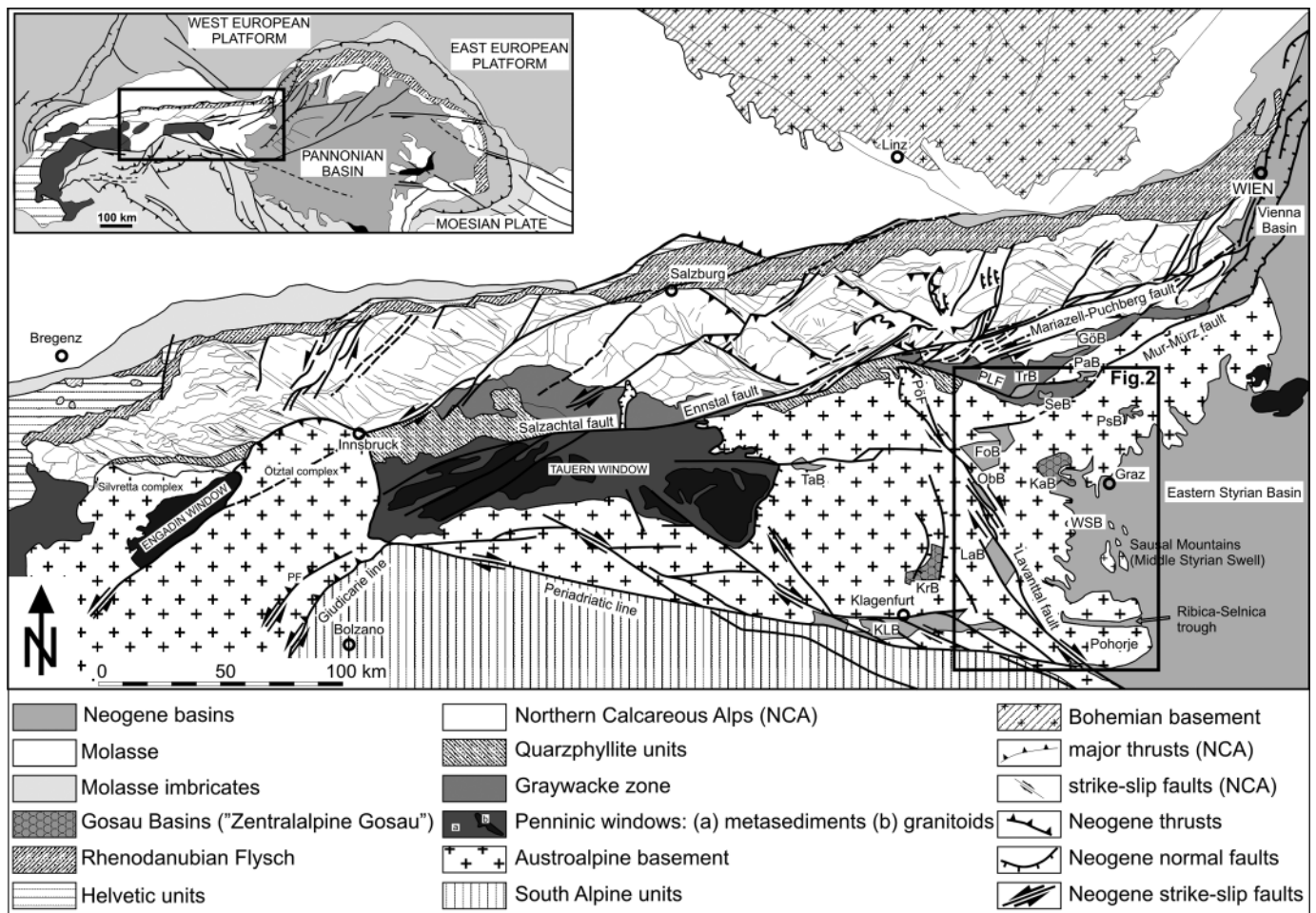
Fig. 1. Tectonic map of the Eastern Alps displaying major and minor Paleogene to Neogene fault systems (after Linzer et al., 2002).
PLF = Palten – Liesing fault; PöF = Pöls fault; GöB = Göriach Basin; PaB = Parschlug Basin; SeB = Seegraben Basin; PSB = Passail Basin; FoB = Fohnsdorf Basin; ObB = Obdach Basin; LaB = Lavanttal Basin; TaB = Tamsweg Basin; TrB = Trofaiach Basin; KLB = Klagenfurt Basin; WSB = Western Styrian Basin; KrB = Krappfeld Gosau Basin; KaB = Kainach Gosau Basin.

insight into the final evolution of the Koralm Complex during the Late Miocene.

2 Geological setting

The major part of the Central Austroalpine nappe pile in the Eastern Alps was already near to the surface during early Cenozoic times, as indicated by zircon and apatite fission track data; these parts were referred to as "Cold Spots" by Hejl (1997). One of these "Cold Spots" is represented by the Koralm Complex (Figs. 1, 2). The pre-Cenozoic evolution of this unit is very well documented by detailed petrological studies (for review, see Habler & Thöni 2001; Kurz & Fritz 2003; Schuster & Kurz 2005). It is characterized by a poly-metamorphic history with signatures of pre-Alpine events and reached amphibolite to eclogite facies conditions during the Cretaceous (Eo-Alpine event). At least three metamorphic events (Variscan, Permian and Cretaceous) are described. The units within the Koralm, Po-

horje, Saualm, and Gleinalm expose high-grade metamorphic units of the Austroalpine Nappe Complex, being incorporated into the Austroalpine nappe stack during the Early Cretaceous (Frank 1987). These units are part of the Lower Central Austroalpine, and in particular the Koralpe – Wölz nappe system (see Janak et al. 2006 and Schmid et al. 2004, respectively) and were formerly referred to as part of the "Middle" Austroalpine unit. These are surrounded by low-grade metamorphic Austroalpine basement units, represented by the Graz Paleozoic in the east, and the Gurktal Nappe in the west, both being part of the Upper Central Austroalpine nappe system and the Drauzug-Gurktal nappe system in particular (see Janák et al. 2006 and Schmid et al. 2004, respectively), formerly referred to as "Upper" Austroalpine. These units are overlain by clastic sediments of Late Cretaceous to Eocene age. Remnants of these clastic sequences are exposed within the Gosau Basins of Kainach and Krappfeld, deposited on top of the Graz Paleozoic and the Gurktal Nappe, respectively (Figs. 1, 2). Alpine cover

sequences, building up the main part of the Northern Calcareous Alps, were detached together with their former basement (the Graywacke Zone) from the units below and were thrusted towards north during the Lower Cretaceous. Thus, the units exposed in the eastern central part of the Eastern Alps particularly document the structural evolution of the Austroalpine basement units and the metamorphic evolution related to the Eo-Alpine collision and subsequent exhumation.

Nappe stacking, HP metamorphism and subsequent exhumation of HP units mainly occurred during the Cretaceous and are referred to as Eo-Alpine evolution (Kurz & Fritz 2003).

Petrological and structural studies (for review see Kurz et al. 2002; Kurz & Fritz 2003), including geochronological work, facilitated a detailed reconstruction of the pressure-temperature-time evolution, in particular from the Permian to the Late Cretaceous. At upper crustal levels, the exhumation of the Koralm Complex was accommodated by low-angle normal faults along its southern and north-eastern margins. Extension accommodated by these normal faults triggered the formation of the Gosau sedimentary basins (Fig. 2) during the Late Cretaceous as well (for a review, see Kurz & Fritz 2003). However, the Koralm Complex was not exhumed to the surface at that time as
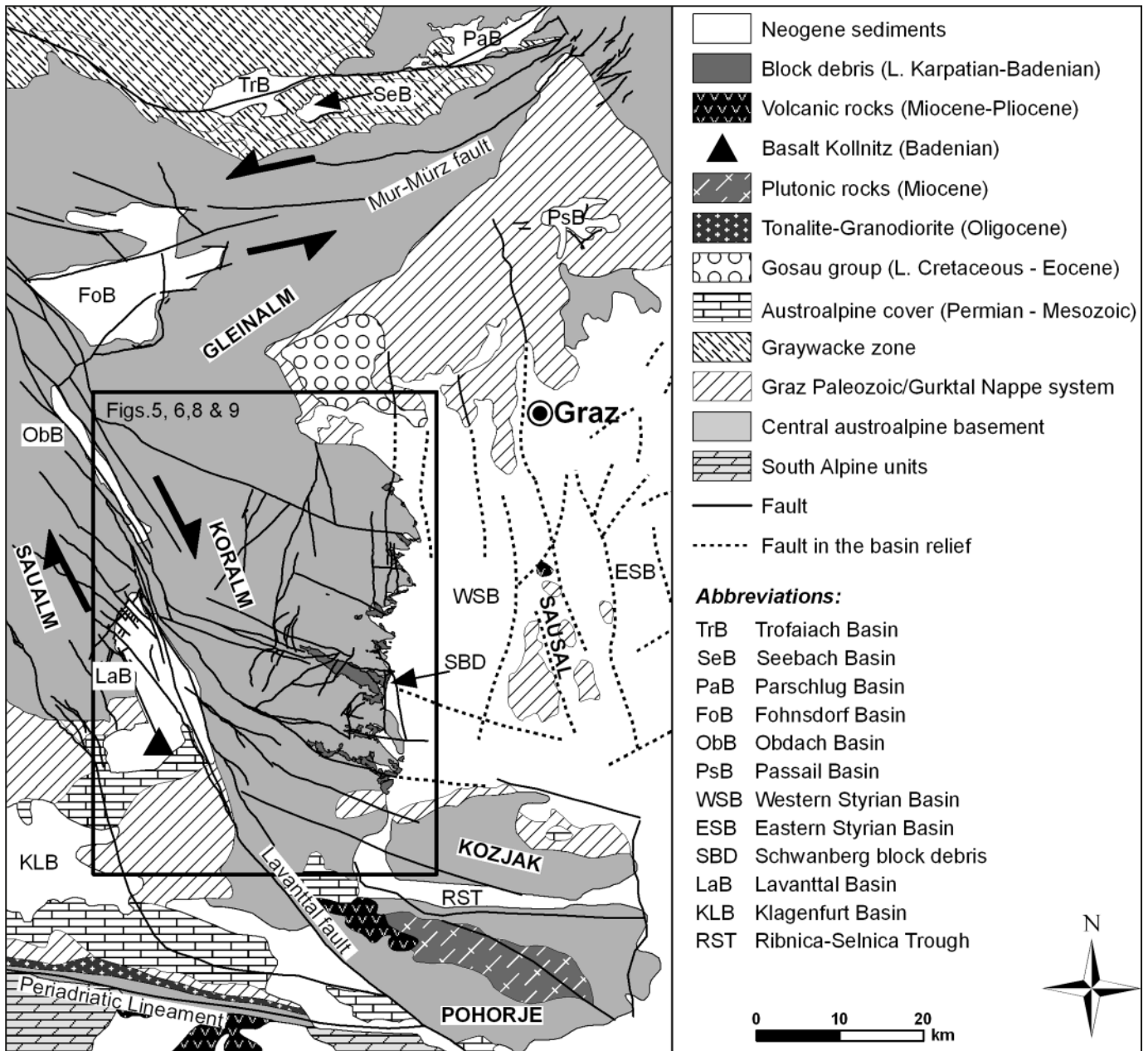
Fig. 2. Geological map of the Koralm Massif and adjacent areas, including the main faults activated during the Miocene.

is indicated by the absence of Koralm-derived pebbles in the Gosau deposits.

The Koralm Complex forms a dome structure with an approximately E–W-trending axis (Kurz et al. 2002). This structure is traced by a penetrative foliation ($s_{1,2}$) dipping to the south in the southern part of the Koralm Complex and the Plankogel Complex, and to the north to northeast in the northern parts; in the central part the penetrative foliation has a subhorizontal orientation. Generally, the foliation is parallel to the lithological and tectonic boundaries, in particular along the southern and northern/northeastern margin of the Koralm Complex.

2.1 Mesozoic/Cenozoic boundary and Cenozoic evolution

The Late Cretaceous to Paleogene tectono-metamorphic evolution of the Koralm Complex and adjacent areas is discussed by Bojar et al. (2001), Fritz et al. (2002), and Kurz & Fritz (2003). The effect of Late Cretaceous to Early Paleogene tectonics and metamorphism is still under debate. Recognition of post-Eoalpine structures and metamorphic assemblages is hampered by the fact that the spatial distribution of Cretaceous/Paleogene structural elements coincide frequently with later, Miocene structures. However, from geochronological and tectono-metamorphic arguments there is strong evidence that the evolution during the latest Cretaceous and Paleogene played a major role in Alpine architecture. This includes: (1) Major tectonic lines, interpreted as Early Cretaceous thrusts are overprinted and sealed by upper greenschist- to amphibolite-facies metamorphism and tectonics. (2) Large rock volumes within eastern sectors of the Eastern Alps cooled down below ca. 250 °C already in Cretaceous times. (3) A large number of geochronological mineral formation ages, previously interpreted to date Eo-Alpine nappe stacking, cluster around *ca.* 80 Ma and may easily be re-interpreted in terms of strike-slip and/or extensional tectonics. In particular, sets of ductile strike slip and normal faults are traced along the southern margin of Austroalpine units (Kurz & Fritz 2003), although frequently obliterated by younger tectonic events along the Periadriatic Lineament (Fig. 1).

Along its margins, the Koralm Complex is surrounded by distinct faults and shear zones. In particular, low-angle normal faults form the northeastern and southern margins of the Koralm Complex. The western margin is formed by a NNW-trending strike slip fault, the Lavanttal fault (Figs. 1, 2). This fault is part of the Pöls-Lavanttal fault system (Frisch et al. 2000a; Reinecker 2000). Along the Lavanttal segment, dextral offset of approximately 10 km was deduced from displaced lithological units. Vertical offset is 4–5 km, whereby the eastern block (Koralm) was up-faulted (Frisch et al. 2000a). Near its southern termination, the Lavanttal fault cuts and offsets the Periadriatic fault by about 20 km. Sedimentary basins (Lavanttal Basin, Obdach Basin) formed along left-handed oversteps. The nature of the Lavanttal Basin is probably an oblique graben structure formed in a transtensional regime (Frisch et al. 2000a); it is assumed to be active since the Early Miocene with peaks in activity between 18–16 Ma and 14–12 Ma (Reinecker 2000). Fault plane solutions display clear dextral strike-slip movements (Reinecker & Lenhardt 1999; Reinecker 2000).

Little is known about the eastern margin of the Koralm Complex, the greatest part of it being hidden below Miocene sediments of the western Styrian Basin (Fig. 1). However, brittle faults and fault-related cataclastic rocks were detected by cored drillings located at the eastern margin of the Koralm Complex (Vanek et al. 2001; Brosch et al. 2001; Pischinger et al. 2005, 2006). Brittle structures that are related to the latest evolution of the Koralm Complex were analysed by Vanek et al. (2001). The few results of tectonic and stress-strain analyses may be correlated with the latest tectonic evolution of the Eastern Alps from the Neogene onwards; this includes sustained N–S-directed extension, being re-oriented and replaced by E–W extension and E–W compression.

Following the descriptions above, the latest clearly documented event within the Koralm Complex is the amphibolite facies metamorphic overprint which occurred at approximately 90 Ma ago. Subsequent cooling is ill-constrained. The final increment of the pressure-temperature-time evolution of the Koralm Complex, i.e. from approximately 90 Ma onwards, is poorly documented, as is the Cenozoic structural evolution of the Austroalpine crystalline complexes in the eastern part of the Eastern Alps. This evolution primarily comprises exhumation, tectonic uplift and surface uplift.

A few data show that crustal stretching, extension and the formation of the Gosau Basins of the Eastern Alps east of the Tauern Window ("Zentralalpine Gosau") coincides with the exhumation of crystalline basement complexes of the Lower Central Austroalpine unit (Fig. 1) (Neubauer et al. 1995). Exhumation resulted in cooling from initial epidote-amphibolite/upper greenschist facies conditions to temperatures below 300 °C at the beginning of the Paleogene. Sphene, zircon and apatite fission track data, for example from the Gleinalm area north of the Koralm Massif, indicate cooling to temperatures below 200–250 °C at 65 Ma (Neubauer et al. 1995). The northern part of the Koralm Complex cooled to temperatures below 200 °C already in the Late Cretaceous (Hejl 1997, 1998). Hence, these regions were already near (approximately 5–8 km) to the surface during the whole Cenozoic. Towards south, the apatite fission track ages within the Koralm Complex gradually become younger. This indicates that the southern parts were exhumed later. In the central part of the Koralm Complex these ages range from approximately 50 to 37 Ma (Hejl 1998; Rabitsch et al. 2007). Approximately 31 Ma are reported from the southern margin of the Koralm Complex, approx. 26 Ma from the western margin (Hejl 1998). Two apatite fission track ages from the central part of the Koralm Complex, close to the Lavanttal fault, show cooling below approximately 120 °C between 28.5 and 18 Ma. West of the Lavanttal fault, apatite fission track ages range from approx. 27 to 12 Ma (Puch 1995). In the Pohorje region early to mid-Miocene cooling of both magmatic and metamorphic rocks is indicated by zircon fission track ages of 26–19 Ma (Fodor et al. 2003). Toward west, in the Gurktal

Nappe Complex (Fig. 1), stronger post-Cretaceous denudation can be observed as compared to the Koralm Complex.

Indirect evidence for the Neogene evolution of the Koralm Complex may be provided by the sedimentary record within the adjacent sedimentary basins (in particular the Styrian and Lavanttal Basins) (Figs. 1–3). The subsidence history of the Styrian Basin as well as that of the Lavanttal Basin, are better constrained due to a well documented stratigraphy (for a summary, see Ebner & Sachsenhofer 1995; Sachsenhofer et al. 1997, 2001). Subsidence started probably at 18 Ma (Ottnangian stage of the Central Paratethys paleogeographic realm) (Fig. 3), followed by a phase of transgression in the Early Karpatian (approx. 17 Ma). In the latest Karpatian (approx. 16.4 Ma) a tectonic event led to the re-organisation of the basin architecture. This event is assumed to be related to block-tilting causing an uplift of the hinterland, represented by the Koralm Massif. This coincided with an eustatic sea level low stand, thus forming a tectonically enhanced sequence boundary. In the southern part of the western Styrian Basin, close to the Pohorje Mountains (Fig. 1), early Miocene sediments lacking a thermal overprint contain apatite grains showing a cooling age of approx. 19 Ma (Eggenburgian), only 1–2 Ma older than the time of deposition (Sachsenhofer et al. 1998). The cooling rate of the mainly Austroalpine source was very fast, pointing to tectonic denudation (Sachsenhofer et al. 1998).

The earliest Badenian (approx. 16 Ma) is characterised by shallow marine conditions; fluvial sedimentation was restricted to the western margin of the basin, i.e. close to the eastern margin of the Koralm Massif. A major sea-level drop at the end of the Badenian (approx. 13 Ma) caused the progradation of (braided-) delta deposits into the western part of the Styrian Basin, followed by a new phase of transgression during the Sarmatian (13–11.5 Ma). This marine influence prevailed up to the Early Pannonian (Sachsenhofer 1996). Limnic and fluviatile sediments replaced this marine period, and from the Late Pannonian onwards, the terrestrial sedimentary influence increased due to continuing uplift.

3 Methods

Slickenside and striae data for paleostress orientation analyses were collected following the methods proposed by Angelier & Mechler (1977) and Angelier (1979) both in the field and, due to the restricted occurrence of adequate outcrops, from drill cores. Within the scope of the geological and geotechnical site investigations for the Koralm Tunnel (with a length of 32.8 km to be built under the Koralm Massif) (Steidl et al. 2001) an enormous volume of data and material has been gained and elaborated during the last years. Especially seven deep core drillings (being part of the site investigations for the Koralm Tunnel), reaching depths of up to 1200 m, have extended the access to geological samples into the third dimension.

Criteria used to determine the sense of slip along brittle faults were described by Petit (1987), Angelier (1994) and Doblas (1998). The collected fault-striae data were consecutively used for paleostress analysis. Analysis was performed for each individual outcrop to keep control on possible overprinting relationships and multistage formation of shear fractures and faults. Only rarely data from nearby outcrops were analysed together, and only in cases when the data sampled were too few at a distinct station and provided that the data clearly belonged to the same kinematic set. Orientation distributions of distinct fracture sets and geometrical relationships were analysed by using the program package Tectonics FP 1.6.2, a 32-bit Windows™-Software for Structural Geology (Reiter & Acs 1996–2001; Ortner et al. 2002). The PT-method (P: contraction axis; T: extension axis; Turner 1953) or graphical method (Marret & Allmendinger 1990) provided by this software, was used to calculate the orientation of the kinematic axes from the fault-striae data. Prior to analysis the fault-striae data were separated into homogeneous subgroups (Meschede & Decker 1993). The P-, T- and the B (intermediate) axes were calculated for each fault plane – striae data set by assuming an angle Θ of 30° between the compression axis and the respective fault plane. A Θ of 30° has been shown to be a reasonable value for most cases according to the Mohr-Coulomb failure criterion (Meschede 1994). The mean vectors for the kinematic axes were calculated after Wallbrecher (1986) and represent an approximation of the principal stress axes (Ortner et al., 2002). For highly anisotropic rocks showing reactivation of the foliation planes as frictional shears, however, a different Θ angle was applied that previously was determined by a best-fit analysis (see Tab. 1). Additionally, for each data set the principal stress directions and the stress ratios were calculated with the numerical dynamical analysis (NDA; Spang, 1972).

In contrast to the analysis of field data, the kinematic analysis of discontinuities in drill core samples combines geophysical borehole logging and structural stress/strain analysis (Brosch et al. 2001; Vanek et al. 2001). This procedure consists of two steps. During the first, each discontinuity encountered in the drill cores and identified by an acoustic borehole televiewer is examined with respect to its nature, surface markings, mode and sense of wall displacements, fillings and primary (in-depth) aperture (Brosch et al. 2001). For linear surface markings (striae) the rake angle is recorded with respect to the relative strike line of the discontinuity in the drill core. Secondly, the rake data are transposed into dip and dip direction data and corrected for the deviation of the borehole from the vertical axis. Then the theoretical compression and tension axes are calculated as described above.

4 Brittle Structures and their interpretation

Morphologically the eastern part of the Koralm Massif is characterised by valleys of two main orientations, either trending N–S or WNW–ESE; the widest of the latter contains the Schwanberg block debris (Fig. 2). These morphological features coincide with the two main sets of brittle structures, in particular fault zones and slickensides, recorded in this area. Therefore it can be assumed that the course of most valleys
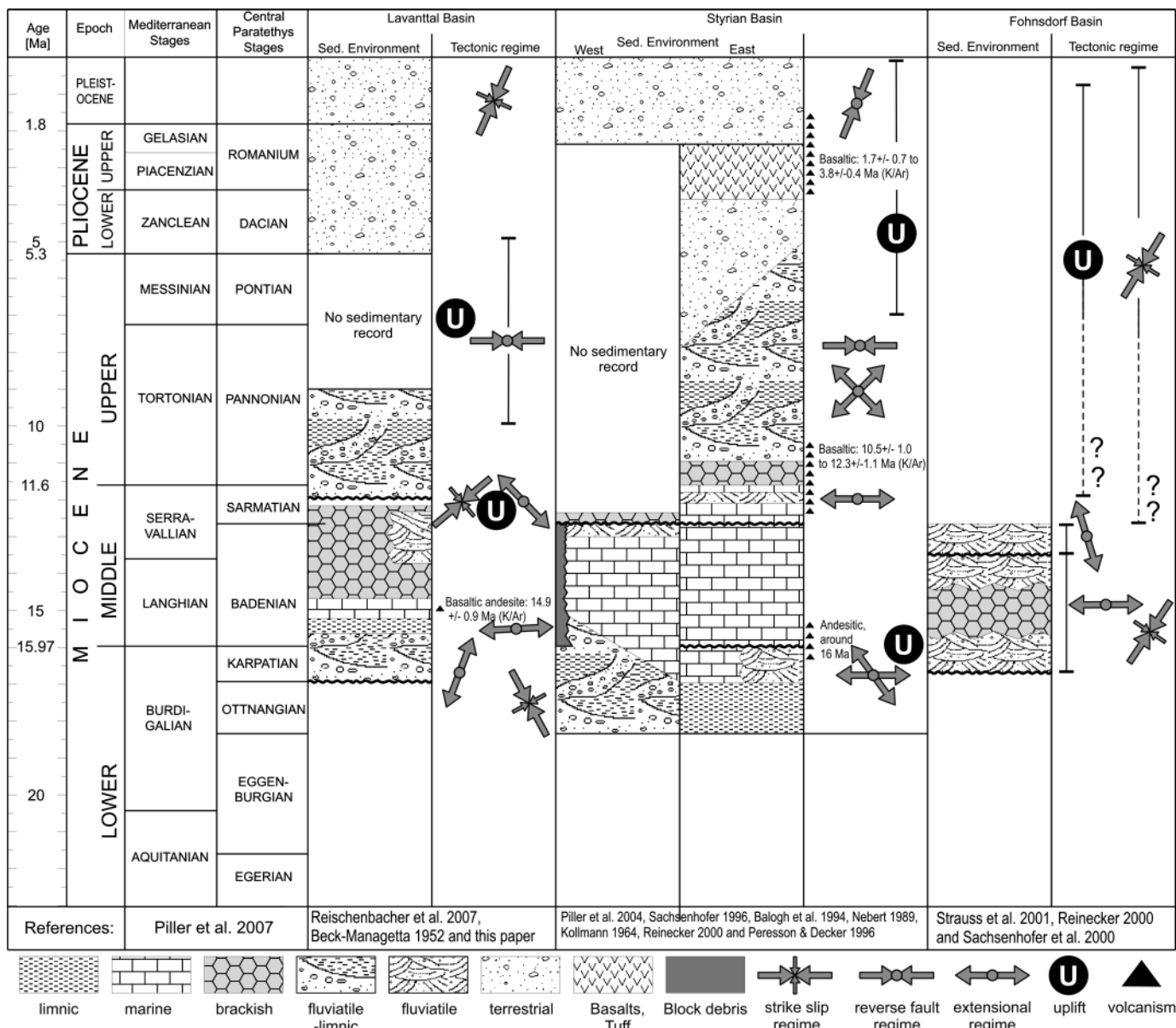
Fig. 3. Comparison of the sedimentary evolution and tectonic regime for the Lavanttal, the Styrian and the Fohnsdorf Basin from the Lower Miocene up to the Pleistocene. Grey filled arrows indicate orientation of paleostress tensors (West is left page margin and East is right page margin).

is fault-controlled, a feature already noted by Stiny (1925) for the northern Koralm. The main faults, together with conjugated secondary fractures, were repeatedly activated during distinct deformational phases.

At map scale mainly two sets of faults can be distinguished; their strike directions range from E to SE and N to NE, respectively (Fig. 2). In general, the E-trending ones are partly covered by block debris deposits; these are crosscut and displaced by NNE-trending faults (Fig. 2). The contact of the Koralm Complex with the Miocene sediments of the western Styrian Basin is badly exposed, as are assumed normal fault zones forming the eastern margin of the Koralm Massif. Both

discontinuities were temporally exposed during the excavation of the Koralm pilot tunnel, showing that the eastern margin of the Koralm Complex is formed by a cataclastic shear zone of approximately 1 meter in thickness in this area (Fig. 4). This zone comprises fine-grained cohesive cataclasites (terminology *sensu* Brodie et al. 2002) with a fragment size of approximately 0.5 to 5 cm; the fragments are embedded within a matrix with predominating grain sizes of 0.2 to 0.5 mm (Fig. 4). A highly fractured damage zone with highly variable thickness (several decimetres to several meters), partly grading into a block-in-matrix rock (*sensu* Medley 1994), characterises the footwall. In the hanging-wall the shear zone is covered by slightly com-
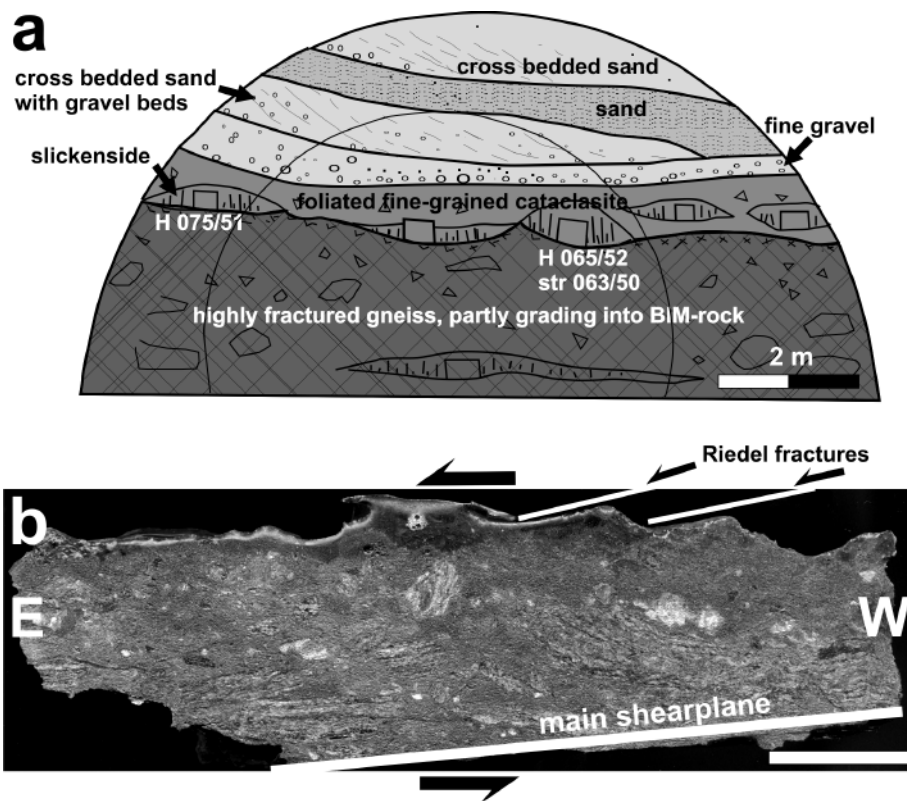
Fig. 4. a) Contact between a cataclastic shear zone and slightly compacted, but undeformed Badenian (?) sand along the eastern margin of the Koralm Complex, as exposed within the pilot tunnel "Leibenfeld" at station 130 m (view is towards east, appr. 12 m wide and 5.5 m high); the cataclastic shear zone rock in the footwall of the sediments is dipping to the east, slickenside striae are plunging subparallel to the fault dip (normal sense of shear); H: slickensided fault plane, str: striation, BIM-rock: Block-in-matrix rock (refer to text for nomenclature). b) polished section of a hand specimen of the cataclasite with gravel-sized, angular to slightly rounded fragments of gneiss in a fine-grained, foliated matrix, Riedel shears support top to east sense of shear. Main shearplane is the same as slickenside in Figure 4a. (Scalebar in the lower right is 3 cm long)

pacted cross-bedded, undeformed sands of probable late Karpatian to early Badenian age (Nebert 1989; Beck-Mannagetta et al. 1991).

At the scale of a few decimetres to meters the sequence of displacements along distinct faults can be derived from over-printing relationships both in outcrops and drill cores. However, these overprinting relationships are restricted to a few key outcrops that provide the basis for the structural analysis at sites with incomplete information about the relative defor-mation sequence. This sequence comprises four major events of brittle deformation, referred to as D_1 to D_4. The coordinates of outcrop locations with detailed data on the orientation of the evaluated principal stress axes are summarised in Table 1.

D_1 can be subdivided into two sub-phases. D_{1-1}-related struc-tures are restricted to distinct domains. Locally, E to ESE strik-ing sub-vertical fractures were activated as dextral strike-slip faults. These are associated with conjugate N to NW-trending dextral, and NNE-trending sinistral strike-slip faults (Figs. 5a, b). A detailed analysis of the distinct stations shows that either ESE and N-trending, or (N)NW and NNE-trending faults oc-cur as conjugate fracture sets. Locally, NW-trending fractures with dextral displacement occur as single sets. The complete assemblage can be geometrically interpreted to represent ESE-trending Y (main)-, E-trending P-, (N)NW-trending R-(Riedel), and NNE-trending R'-fractures. The results from the analysis of paleostress orientations show a sub-horizontal NNW–SSE orientation of σ_1 and a sub-horizontal orientation of σ_3 in ENE–WSW-direction (Figs. 5a, b). The block debris deposits

of Schwanberg, mainly consisting of components derived from the adjacent basement, are related to major D_{1-1}-related ESE-trending faults, too. According to Nebert (1989), sedimentation of these deposits started during the Late Karpatian/Early Bad-enian (Fig. 3). In general, the base of the deposits is formed by a zone of highly disintegrated host rock, often accompanied by the development of tectonic breccias and cataclasites. Adjacent to the block debris deposits, the basement protoliths (mainly garnet mica-schist and schistose garnet-bearing gneiss) show severe alteration and deformational overprint of the pen-etrative fabrics along distinct semi-ductile shear zones. The basement protolith is intensely retrogressed; biotite is mainly replaced by stilpnomelane, plagioclase is mainly replaced by epidote-zoisite and calcite (Egger 2007). Besides the alteration, the development of veins and cracks healed by calcite and sub-ordinate quartz, white mica, and zeolite indicates the presence of hydrothermal fluids during faulting.

The ESE striking dextral strike-slip shears were reacti-vated during D_{1-2} as conjugate high-angle normal faults. This is indicated by sub-vertical striae associated with top-down displacement criteria overprinting the D_{1-1}-related sub-hori-zontal striae (Fig. 5d). These high-angle normal faults are far better preserved than the previous strike-slip faults and are locally associated with the development of cm-thick fault gouges. The main valleys and ridges strike parallel to these WNW–ESE oriented structures. As observed in drill cores the D_{1-2}-related normal faults crosscut the lower parts of the block debris deposits of Schwanberg as well (Egger 2007). The

Table 1. Coordinates of outcrop locations used for paleostress analysis with detailed orientations of the principal stress/strain axes determined for each location. Coordinates are in Austrian BMN M34 system. N – total number of data, Nbiv.. number of bivalent data, PT…PT method after Turner (1953), NDA – numerical dynamical analysis after Spang (1972), secfrac – kinematics deduced from secondary fractures e.g. Riedel fractures, Kex – extension fractures (gashes), con – conjugated shear fractures; P – compression axis, B – intermediate axis, T – extension axis, Theta – angle of internal friction, R – shape factor of the paleostress ellipsoid calculated with the numerical dynamical analysis (NDA) after Spang (1972). PT and NDA were calculated with TectonicsFP (Reiter and Acs 1996–2001).

Outcrop-ID	Easting	Northing	Altitude	Method	N	N$_{biv}$	P [°] dipdir	dip	B [°] dipdir	dip	T [°] dipdir	dip	Theta [°]	R	Event
1	663924	196819	531	PT, NDA	4	0	48	72	275	8	181	15	35	0.435	D1-2
1	663924	196819	531	PT, NDA	15	4	138	83	5	5	280	5	35	0.422	D2
5	663787	192855	695	Extension	3	0	270	89	360	1	90	1			D2
7	643581	186454	1554	PT	3	0	227	79	332	1	61	9	30		D2
7	643581	186454	1554	PT	3	0	236	15	123	55	336	31	30		D3-1
7	643581	186454	1554	PT, NDA	4	0	297	80	28	2	121	10	30	0.578	D3-2
8	647102	190757	1384	PT, NDA	15	3	160	76	283	8	11	14	20	0.455	D1-2
9	647176	190763	1364	PT, NDA	8	3	145	69	306	13	40	6	30	0.487	D1-2
10	647070	190665	1384	PT, NDA	6	0	143	88	293	19	27	10	30	0.539	D1-2
22	644596	182403	1351	PT	3	0	173	21	326	69	79	6	35		D1-1
24	661794	193955	803	PT	4	1	212	43	22	51	303	2	30		D3-1
26	662236	194433	772	PT	3	0	84	81	342	2	251	7	30		D2
30	645204	175958	1159	PT, NDA	5	0	283	75	116	14	24	4	30	0.49	D1-2
47	641508	182275	779	PT, NDA	5	1	222	62	353	17	86	20	30	0.508	D2
49	660446	210288	400	PT, NDA	6	1	123	57	347	24	246	19	30	0.471	D2
49	660446	210288	400	conjug	12	0	143	88	53	1	323	2			D3-2
50	655925	184494	957	PT, NDA	12	4	51	43	193	48	308	16	30	0.519	D3-1
52	662334	198465	480	PT	5	4	33	23	273	83	126	7	30		D3-1
53	662576	198465	480	PT, NDA	5	1	34	41	190	47	292	13	30	0.513	D3-1
69	649017	207767	824	PT	3	0	252	74	156	2	66	17	30		D2
70	649543	207315	821	PT, NDA	4	0	332	69	186	17	93	11	30	0.506	D2
71	653276	203732	941	PT	3	0	343	7	128	89	69	5	30		D1-1
72	654254	204047	944	PT, NDA	6	2	69	80	169	2	256	10	30	0.524	D2
72	654254	204047	944	PT, NDA	9	0	144	1	42	78	234	17	30	0.539	D1-1
73	645808	181306	1385	PT, NDA	7	0	242	54	120	22	17	32	30	0.46	D1-2
74	645026	181295	1156	PT, NDA	10	5	140	82	318	9	47	1	30	0.505	D2
75	641028	173255	351	PT, NDA	22	0	186	11	44	77	277	10	30	0.521	D1-1
75	641028	173255	351	PT, NDA	4	0	319	73	112	14	204	7	42	0.427	D1-2
75	641028	173255	351	PT, NDA	12	0	215	6	96	79	306	10	30	0.502	D3-1
75	641028	173255	351	PT, NDA	15	0	240	87	20	4	110	2	30	0.436	D3-2
76	665673	207869	360	PT, NDA	7	0	193	70	349	19	82	7	30	0.525	D2
78	665609	208009	360	Extension	6		260	89	350	1	80	1			D2
78	665609	208009	360	Extension	3		324	89	54	1	144	1			D3-2
79	656552	183317	1003	extension	7		93	79	183	1	273	11			D2
80	654290	182897	1408	PT, NDA	5	0	62	82	273	8	182	3	30	0.483	D1-2
80	654290	182897	1408	PT	3	0	230	50	23	37	124	15	30		D3-1
83	654524	184073	1104	PT	3	0	335	72	85	5	175	16	30		D1-2
83	654524	184073	1104	PT, NDA	4	0	118	76	215	3	306	15	30	0.504	D3-2
83	654524	184073	1104	PT, NDA	6	0	73	5	187	79	335	8	30	0.528	D3-1
84	656922	183178	962	PT, NDA	11	0	102	75	240	11	332	11	30	0.484	D3-2
87	663564	197707	485	PT	3	0	6	24	217	62	100	9	30		D3-1
87	663564	197707	485	PT	3	0	265	79	357	3	88	11	30		D2
88	663482	198540	519	PT, NDA	8	1	190	83	16	6	286	1	30	0.514	D2
91	664252	199059	483	PT, NDA	7	1	79	77	193	3	288	12	30	0.457	D2
92	663094	199115	604	PT	3	0	184	76	17	13	286	3	30		D2
96	665011	197074	434	PT, NDA	7	0	116	79	10	4	281	11	38	0.496	D2
105	653654	203296	946	PT, NDA	6	1	93	58	264	25	350	7	30	0.502	D1-2
111	644448	183782	1512	PT, NDA	12	0	259	59	45	27	142	15	30	0.46	D3-2
113	643169	180605	916	PT, NDA	22	7	49	73	288	9	198	12	30	0.503	D1-2
114	642505	180715	820	PT, NDA	6	0	89	76	241	12	332	4	30	0.419	D3-2
114	642505	180715	820	PT, NDA	9	0	299	76	129	13	39	3	30	0.518	D1-2
114	642505	180715	820	PT, NDA	8	0	91	15	318	71	187	10	30	0.543	D4
116	643499	190857	787	PT, NDA	16	4	210	56	84	16	345	26	30	0.487	D1-2
116	643499	190857	787	PT	3	0	163	52	5	36	267	11	30		D1-1
117	643312	190960	846	PT, NDA	5	0	175	56	3	36	270	3	30	0.452	D2
118	642288	191188	677	PT, NDA	12	0	258	79	65	13	155	5	30	0.416	D1-2
122	641852	191822	835	PT, NDA	9	1	166	67	31	17	295	16	30	0.503	D3-2
125	641585	191533	708	extension	5	0	121	59	31	1	301	31			D3-2
127	641605	191508	670	PT	3	1	126	58	35	9	292	31	30		D3-2

Table 1. (Continued).

Outcrop-ID	Easting	Northing	Altitude	Method	N	N$_{biv}$	P [°] dipdir	dip	B [°] dipdir	dip	T [°] dipdir	dip	Theta [°]	R	Event
129	641008	191033	796	PT, NDA	10	0	153	22	14	62	248	16	30	0.398	D1-1
129	641008	191033	796	PT, NDA	6	0	133	64	12	10	278	22	30	0.443	D2
133	640619	191656	582	PT, NDA	13	2	13	1	172	88	284	2	46	0.412	D3-1
134	643312	190960	846	PT, NDA	19	0	295	72	26	0	114	17	32	0.503	D3-2
134	643312	190960	846	PT, NDA	5	0	206	33	7	56	110	7	42	0.502	D3-1
134	643312	190960	846	PT	3	0	315	40	156	46	53	12	32		D1-1
137	643185	189360	1264	PT, NDA	8	2	152	32	11	47	254	23	30	0.522	D1-1
137	643185	189360	1264	PT, NDA	6	1	231	78	111	6	18	7	30	0.504	D1-2
140	643147	189657	1290	kex, conjug	4	0	192	59	31	29	296	6			D3-2
142	662283	197361	687	PT, NDA	18	0	111	86	10	1	284	4	30	0.412	D2
142	662283	197361	687	PT, NDA	5	0	177	21	328	69	82	15	30	0.587	D1-1
147	646630	164609	420	PT	3	1	342	51	171	49	83	0	30		D1-1
153	643033	184644	1299	PT, NDA	6	0	285	85	109	4	20	1	30	0.524	D1-2
153	643033	184644	1299	PT, NDA	8	0	159	72	344	18	253	2	30	0.503	D2
153	643033	184644	1299	PT	4	3	193	12	25	58	98	22	30		D3-1
155	642137	172272	431	PT	5	3	317	4	209	70	48	6	30		D1-1
158	661345	184999	610	PT	3	0	71	81	184	4	274	9	30		D2
160	661532	184990	627	PT	3	0	268	71	100	19	9	4	30		D1-2
161	655900	187379	950	PT, NDA	8	0	225	76	3	10	94	9	30	0.515	D2
163	660863	185328	593	PT, NDA	9	1	129	79	5	7	276	9	30	0.492	D2
164	658552	185624	728	PT, NDA	7	1	69	1	155	0	221	89	70	0.49	D4
164	658552	185624	728	PT, NDA	5	0	4	4	239	82	92	7	30	0.487	D1-1
166	666079	194998	552	PT, NDA	14	0	355	65	139	21	234	9	30	0.483	D2
166	666079	194998	552	PT, NDA	7	3	289	18	83	70	197	8	30	0.516	D4
167	666222	195122	495	Extension	6	0	250	89	160	1	70	1			D2
172	657335	206228	624	PT	3	0	32	78	169	8	261	11	30		D2
173	662431	209863	393	PT, NDA	7	0	129	53	277	32	17	16	30	0.495	D1-2
175	636706	197628	647	PT, NDA	8	3	179	16	320	69	87	9	30	0.501	D1-1
175	636706	197628	647	PT	5	2	66	74	330	2	240	14	30		D2
177	638417	195115	584	PT	3	0	156	18	13	68	251	14	30		D1-1
177	638417	195115	584	PT	3	0	210	62	90	14	352	22	30		D1-2
178	636596	197512	620	PT	3	1	196	61	329	32	76	17	30		D2
186	660723	191011	515	PT, NDA	9	0	9	11	187	78	278	2	30	0.538	D1-1
187	659822	191359	568	PT	5	2	132	74	12	5	282	19	20		D3-2
187	659822	191359	568	PT, NDA	13	4	0	3	98	77	271	7	20	0.668	D1-1
190	663218	184495	771	PT	7	4	345	3	10	89	75	1	25		D1-1
192	637814	199201	717	PT, NDA	6	0	143	51	8	30	263	22	30	0.507	D2
193	638250	199468	717	PT	3	0	332	28	75	23	195	51	30		D1-1
195	644347	179775	1034	PT, NDA	6	1	350	82	111	8	204	8	30	0.447	D1-2
204	657747	193401	667	PT, NDA	5	1	345	73	153	14	250	2	30	0.474	D2
207	660402	191534	519	PT	3	1	29	13	287	52	126	27	30		D3-1
214	659807	191581	501	PT	6	4	352	12	158	73	262	2	30		D1-1
215	664345	185080		PT, NDA	8	0	88	78	349	2	258	12	30	0.46	D2
216	663811	184927		PT	4	3	176	5	336	71	85	17	30		D1-1
220	650377	182333	1574	PT	3	0	129	23	263	61	30	19	30		D1-1
222	659330	185505	681	PT, NDA	6	1	150	5	21	79	239	11	30	0.511	D1-1
223	660685	184075	630	PT, NDA	7	0	113	82	290	10	20	4	30	0.489	D1-2
224	639826	199759	730	PT,NDA	10	0	320	7	53	45	222	41	30	0.493	D1-1
224	639826	199759	730	PT, NDA	4	0	123	53	310	38	217	2	30	0.483	D1-2
225	633483	185458	472	PT	5	3	73	9	287	69	164	10	30		D3-1
226	663955	184694	563	PT	29	7	108	50	344	27	238	27	45		D2
226	663955	184694	563	PT	6	0	338	78	81	2	172	11	40		D1-2
227	663183	184861	664	PT	27	3	205	55	23	39	111	4	40		D3-2
227	663183	184861	664	PT	3	0	125	60	312	30	218	6	30		D1-2
227	663183	184861	664	PT	4	0	7	14	99	18	240	71	30		D3-1
228	658129	183153	650	PT	19	0	46	52	167	22	271	30	35		D2
228	658128.5	183153	650.455	PT	15	0	121	70	237	8	329	18	32		D3-2
228	658128.5	183153	650.455	PT	17	0	340	77	102	9	188	14	35		D1-2
229	655507.6	185555.5	981.77	PT	12	0	253	71	87	19	352	7	32		D1-2

high-angle faults are additionally associated with sub-vertical, ESE striking extensional veins and open fractures, indicating (N)NE-(S)SW-directed extension. This interpretation is supported by the paleo-principal stress orientations, i.e. σ_1 with a sub-vertical orientation, σ_3 with a (N)NE – (S)SW orientation (Fig. 5c).

Table 1. (Continued).

Outcrop-ID	Easting	Northing	Altitude	Method	N	N$_{biv}$	P [°] dipdir	P [°] dip	B [°] dipdir	B [°] dip	T [°] dipdir	T [°] dip	Theta [°]	R	Event
229	655507.6	185555.5	981.77	PT	8	0	197	18	96	38	305	47	26		D3-1
230	649069.8	184805.2	1465.56	PT	9	0	251	75	70	13	165	3	30		D1-2
230	649069.8	184805.2	1465.56	PT	18	0	72	81	18	1	282	13	40		D2
231	644176.6	183776	1473.04	PT	4	2	180	51	14	29	281	11	35		D2
232	642857.9	182093.9	926.372	PT	10	2	184	79	277	6	16	14	38		D1-2
232	642857.9	182093.9	926.372	PT	9	2	172	67	2	8	271	4	38		D2
233	659741.8	183436.5	930.21	PT	22	0	12	74	113	4	196	15	26		D1-2
233	659741.8	183436.5	930.21	PT	16	0	43	65	216	25	306	7	36		D3-2
233	659741.8	183436.5	930.21	PT	18	0	15	4	105	49	296	45	30		D3-1
233	659741.8	183436.5	930.21	PT	12	0	88	7	171	29	338	56	30		D4
234	651250.7	183919.2	1510.56	PT	60	0	301	86	99	5	189	5	35		D1-2
234	651250.7	183919.2	1510.56	PT	91	0	178	69	3	24	272	3	46		D2
234	651250.7	183919.2	1510.56	PT	13	0	155	17	54	30	265	54	35		D1-1
234	651250.7	183919.2	1510.56	PT	6	0	255	2	354	61	157	29	35		D3-1
235	641981.6	180586.5	700.67	PT	13	0	350	76	100	4	189	14	50	0.507	D1-2
235	641981.6	180586.5	700.67	PT	18	0	355	78	154	12	245	0	52	0.498	D2
235	641981.6	180586.5	700.67	PT	12	0	47	81	229	9	138	2	64	0.542	D3-2
236	656711	181761.2	1233.02	PT	19	0	150	33	13	49	252	23	40	0.511	D1-1
236	656711	181761.2	1233.02	PT	12	0	213	71	91	11	356	13	30	0.564	D1-2
236	656711	181761.2	1233.02	PT	5	0	109	77	330	10	241	8	42	0.53	D2
236	656711	181761.2	1233.02	PT	4	0	52	17	266	72	146	9	30	0.231	D3-1
236	656711	181761.2	1233.02	PT	6	0	211	0	113	2	107	86	40	0.48	D3-1
237	650458.8	181155	1374.76	PT	3	0	162	3	284	87	76	2	30		D1-1
237	650458.8	181155	1374.76	PT	16	0	142	69	355	18	259	11	30	0.505	D2
237	650458.8	181155	1374.76	PT	21	0	158	19	46	50	258	34	30	0.503	D1-1
237	650458.8	181155	1374.76	PT	7	0	50	12	190	72	324	11	20	0.567	D3-1
237	650458.8	181155	1374.76	PT	26	0	197	51	35	38	299	10	30	0.519	D3-2
238	647255.7	180773	1581.38	PT	4	0	217	66	80	17	347	15	30	0.443	D1-2
238	647255.7	180773	1581.38	PT	5	0	68	21	333	11	216	66	30	0.475	D4
238	647255.7	180773	1581.38	PT	3	0	201	1	111	29	292	60	30		D3-1
238	647255.7	180773	1581.38	PT	3	0	164	16	52	56	256	32	30		D1-1
238	647255.7	180773	1581.38	PT	18	0	246	66	99	21	4	13	48	0.464	D1-2
238	647255.7	180773	1581.38	PT	25	0	253	70	29	13	123	13	54	0.452	D3-2
238	647255.7	180773	1581.38	PT	3	0	217	7	128	11	339	79	30		D3-1
239	647255.7	180773	1581.38	PT	9	0	258	73	40	14	132	17	68	0.578	D3-2
239	647255.7	180773	1581.38	PT	4	0	280	67	125	17	38	6	54	0.516	D1-2
240	654045.3	181267	1545.4	PT	55	0	137	72	347	15	255	11	50	0.448	D2
240	654045.3	181267	1545.4	PT	3	0	220	12	99	64	314	22	30		D3-1
240	654045.3	181267	1545.4	PT	13	0	254	60	39	23	133	17	78	0.485	D3-2
240	654045.3	181267	1545.4	PT	6	0	186	75	33	13	302	6	30	0.433	D3-2
240	654045.3	181267	1545.4	PT	7	0	218	61	44	30	313	2	80	0.47	D3-2
240	654045.3	181267	1545.4	PT	5	0	100	15	2	24	212	63	20	0.465	D4

Most of the brittle structures observed in the southern part of the Koralm Massif are related to D$_2$. These are N–S striking slickensides, the major set steeply dipping towards E, and minor conjugate sets dipping to the W (Fig. 6). Slickenside – related striae plunge subparallel or slightly oblique to the slickenside dip direction and show top-down kinematic indicators. In the field these shear fractures are locally associated with sub-vertical extensional veins arranged within an en echelon geometry, mainly filled with quartz or calcite. As seen particularly in drill cores, sub-vertical open en echelon fissures strike in a N–S direction. Altogether, these structures can be interpreted as being related to general E–W-directed extension; they dominate both in surface exposures and in drill cores. The results from the analyses of paleostress orientations show a sub-vertical orientation of σ$_1$, and a sub-horizontal orientation of σ$_3$ in E–W to ESE–WNW-direction, locally shifting to a (N)NW-(S)SE orientation (Fig. 6).

These high-angle structures are repeatedly associated with E-dipping low-angle normal faults and shear zones. The latter formed by the reactivation of the penetrative foliation, mainly within smoothly dipping Plattengneis domains. These shear zones are accompanied by cataclastic fault rocks, consisting of very fine grained quartz, white mica and biotite in the matrix with incorporated broken grains of feldspar or cm to decimetre large protolith fragments (Fig. 7a). The damage zone (*sensu* Chester & Logan 1986; Caine et al. 1996) adjacent to the low-angle shear zones is characterised by the formation of closely, millimetre- to centimetre-spaced fractures, 5–20 cm in length, at high angles (70–90°) to the fault zone boundaries, bounding distinct rhombohedral blocks. The fracture-bound blocks show antithetic bookshelf rotation referring to the displacement along the low-angle shear zones, and associated to normal displacement along the high-angle fractures, too (Fig. 7b). Locally
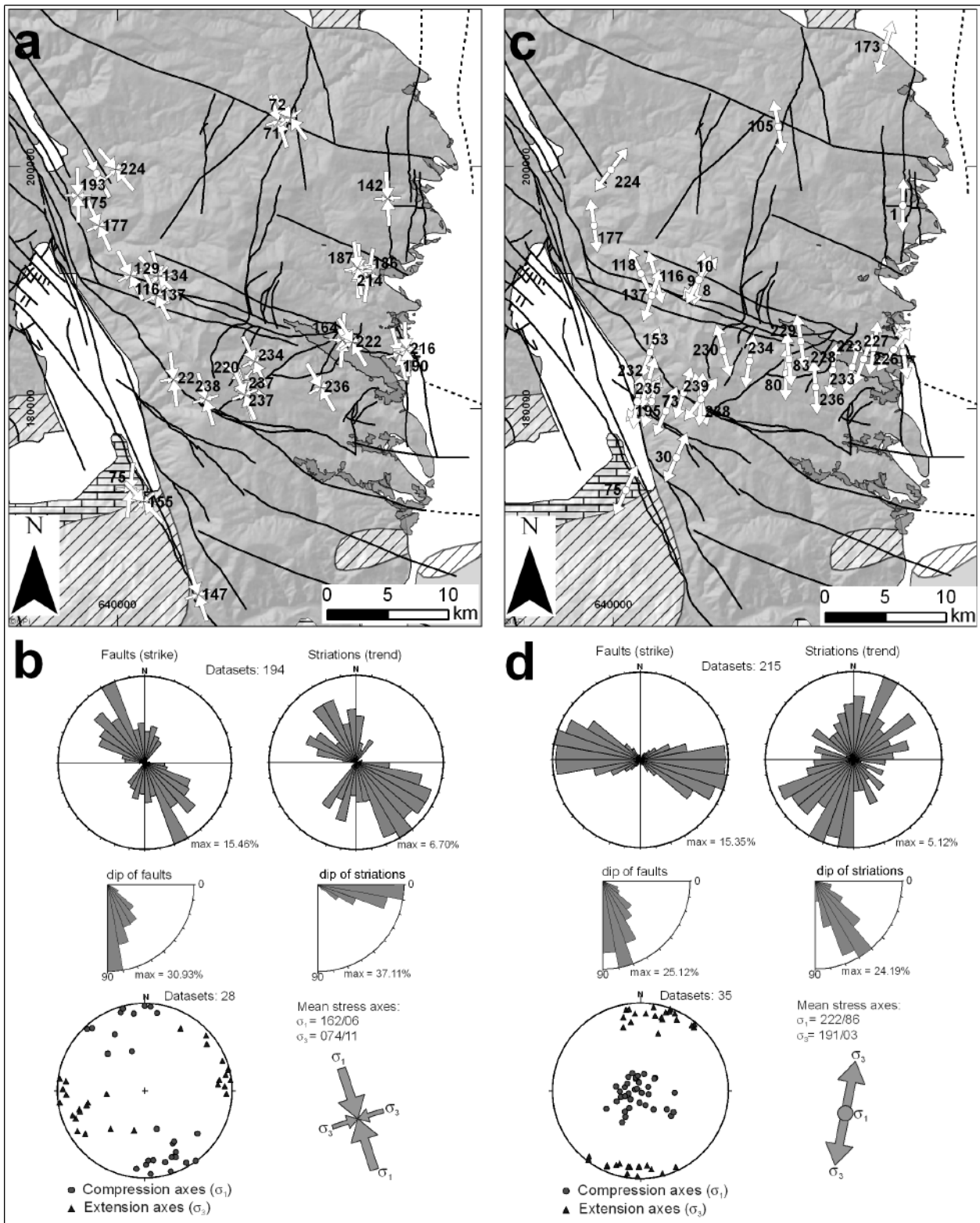
Fig. 5. a) Orientation of σ_1 (large arrows) and σ_3 (small arrows) related to D_{1-1}; labeled numbers refer to Table 1. b) Rose diagrams with strike and dip of fault planes and trend of striations; orientation of σ_1 (filled circles) and σ_3 (triangles) of D_{1-1}-related tensors with mean maximum and minimum principal stress axes. c) Orientation of σ_1 (large arrows) and σ_3 (small arrows) related to D_{1-2}; labeled numbers refer to Table 1. d) Rose diagrams with strike and dip of fault planes and trend of striations; orientation of σ_1 (filled circles) and σ_3 (triangles) of D_{1-2}-related tensors with mean maximum and minimum principal stress axes. Refer to Figure 2 for legend of geological units. Grid is in Austrian BMN M34 system.

these low angle shear zones are associated with antithetic W-dipping conjugate high-angle normal faults (Fig. 7a). Synthetic sets of high-angle fractures continuously curve into the dip direction of the low-angle shear zones and form listric normal faults. Towards the lower tip line the high-angle faults show the development of cataclasites. High disintegration of the protolith may be observed along antithetic high-angle faults, too; in most cases, however, the original structure of the protolith can still be identified, irrespective of the slight alteration of the protolith. This alteration is characterised by the enrichment of feldspar and biotite. Around the upper tip area, the high-angle faults may split up into splays, typically forming horse-tail structures.

N–S striking D_2-related major faults crosscut both previously formed E- to SE trending faults and the block debris deposits of Schwanberg. Locally, the block debris is crosscut by distinct brittle shear zones, a few centimetres wide, as well as by slickensides, indicating a post-sedimentary (re-)activation of distinct faults.

D_3 is characterised by a sub-horizontal orientation of the minimum principal stress σ_3 in SE–NW direction (Fig. 8). Lo-

cally, E–W trending fractures are activated as sinistral shears. Additionally ENE- and NNW-striking subvertical fractures are activated as strike slip planes with sinistral and dextral sense of shear, respectively. A detailed analysis of single stations shows that (E)NE- and N- to NW-trending fractures may occur as conjugate shears. The complete assemblage can be geometrically interpreted to represent E-trending Y-, NE-trending R-, and (N)NW-trending R'-fractures (Figs. 8a, c). The analysis of paleostress orientations for this deformational event (D_{3-1}) indicates a sub-horizontal NE–SW orientation of the maximum, and a sub-horizontal NW–SE orientation of the minimum principal stress axis (σ_1 and σ_3, respectively) (Figs. 8a, b). Locally, mainly along restraining bends along E–W-striking strike slip faults, σ_3 shifts to a subvertical orientation. This indicates inversion of previously formed E-trending faults and related basins. However, these orientations are poorly constrained because of lack of sufficient data due to subsequent reactivation of fault planes.

SSE to S striking fractures were reactivated as oblique high-angle normal faults with striae dipping toward NW and SE, respectively (D_{3-2}) (Fig. 8d). Foliation planes slightly dipping to
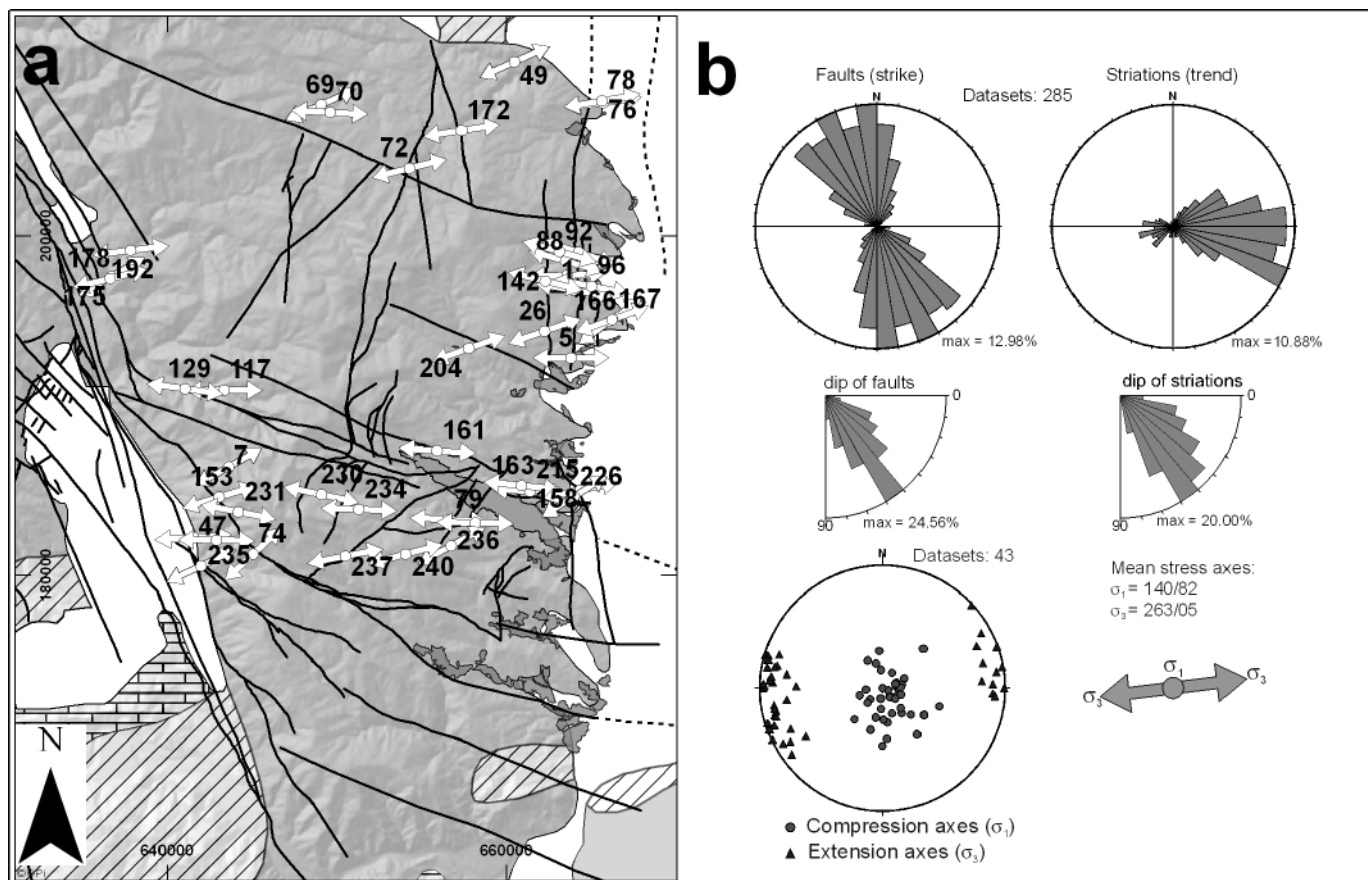
Fig. 6. a) Orientation of σ_1 (large arrows) and σ_3 (small arrows) related to D_2; Labeled numbers refer to Table 1. b) Rose diagrams with strike and dip of fault planes and trend of striations; orientation of σ_1 (filled circles) and σ_3 (triangles) of D_2-related tensors with mean maximum and minimum principal stress axes. Refer to Figure 2 for legend of geological units. Grid is in Austrian BMN M34 system.
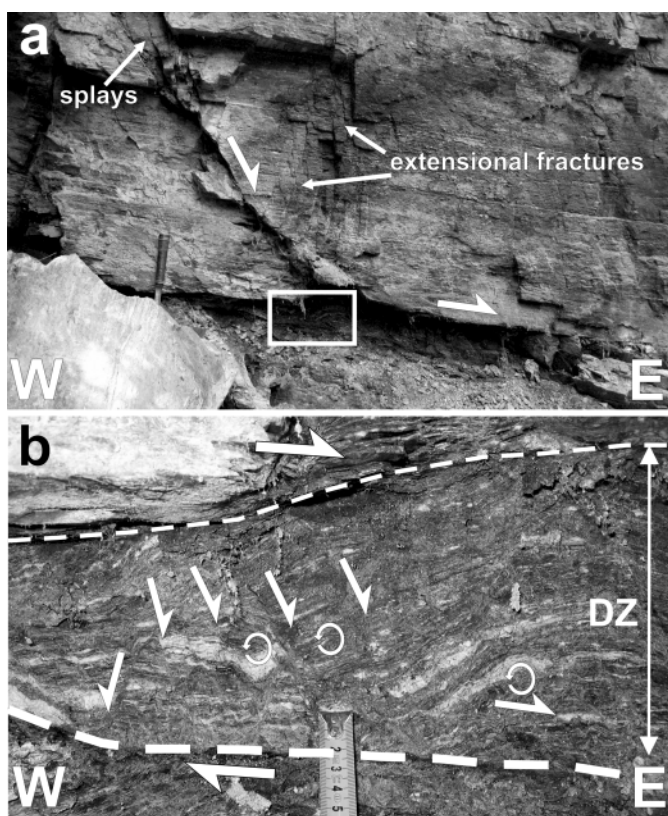
Fig. 7. a) Listric cataclastic shear zone dipping towards E, passing into a shear zone parallel to the foliation of the Plattengneis. White rectangle indicates location of Figure 4b, use hammer handle for scale (approx. 18 cm). b) High-angle fractures associated with foliation parallel cataclastic shear zones with shear-related antithetic rotation of fracture-bound fragments (outcrop-ID: 96, NW of Stainz/Styria).

the E were activated as oblique low-angle normal faults as well. Paleostress orientation analysis of the fault-striae data related to this deformational phase yields a sub-vertical orientation of σ_1 and a sub-horizontal orientation of σ_3 in SE–NW direction (Fig. 8c, d).

Especially sub-horizontal and slightly E- and W-dipping pre-existing foliation planes as well E- and W-vergent low-angle normal faults were finally re-activated as low-angle reverse faults (thrusts) as can be deduced from associated slickensides and striae indicating reverse to oblique reverse slip (D_4; Fig. 9). The displacements range from of a few centimetres to decimetres. The analysis of paleo-principal stress orientations indicates sub-horizontal σ_1 in E–W direction, and sub-vertical σ_3 (Fig. 9). E–W oriented compression is additionally indicated by the development of kink bands (Fig. 10a) and the normal drag of the pre-existing foliation forming s-type flanking folds in terms of Grasemann et al. (2003) (Fig. 10b).

5 Summary and Discussion

The evolution of the eastern part of the Eastern Alps, in particular the Koralm Massif and the adjacent sedimentary basins,

during the Paleogene is not well known due to the sporadic sedimentary record and the rather low abundance of geochronological data from this period. The Miocene tectonic evolution is better documented for the sedimentary basins, in particular the Styrian and the Lavanttal Basin, located to the east and west of the Koralm Massif, respectively. However, the Paleogene and Neogene evolution of the Koralm Complex still lacks a detailed documentation.

In general, this part was transected by two major sets of faults, coinciding with the general Miocene fault pattern of the Eastern Alps (compare e.g. Ratschbacher et al. 1991; Decker & Peresson 1996; Neubauer et al. 2000). These are:

1. ESE–WNW- to E–W-trending faults, associated with ENE- and NNW-trending conjugate structures;
2. N- to NNE-striking faults, mainly acting as high-angle normal faults, often associated with E-dipping low-angle normal faults along the western margin of the Styrian Basin.

These fault sets were multiply (re-) activated during the Miocene, resulting in a complex pattern of fault interferences. Detailed timing of distinct phases of faulting still remains difficult due to the lack of geochronological data directly dating fault activity, and the lack of exposed interference with sedimentary deposits. Especially along the eastern margin of the Koralm Massif, previously formed E-trending faults and associated structures were covered or sealed by syn- to post-tectonic sediments and may hardly be traced toward east into the Styrian Basin. However, together with the stratigraphic and paleogeographic evolution of the Styrian and Lavanttal Basins and the related subsidence histories (see, for example, Weber & Weiss 1983; Ebner & Sachsenhofer 1995; Sachsenhofer et al. 1997, 1998; Dunkl et al. 2005; Vrabec & Fodor 2005) a rough structural evolution, not provided so far, may be reconstructed for this part of the Eastern Alps.

In general, the Koralm Massif, adjacent basement units north and south of it, and the Styrian Basin are bordered by two major confining fault zones: the ESE-trending Periadriatic fault with dextral sense of displacement in the south, and a system of ENE-trending sinistral fault zones in the north (e.g. Neubauer et al. 2000) (Fig. 11). These are linked by the NNW-trending Lavanttal fault system west of the Koralm Massif (Fig. 11). The evolution of the Styrian Basin can be subdivided into an Early Miocene (Ottnangian to Karpatian: approximately 18–17 Ma) synrift phase and a subsequent postrift phase (Ebner & Sachsenhofer 1995). During the synrift phase, there is a close genetic relation between basin formation and the formation of pull apart structures along predominately E-trending strike slip zones (Ebner & Sachsenhofer 1995; Sachsenhofer et al. 1997, 1998).

During a first phase of deformation (D_{1-1}) WNW–ESE-striking fractures were activated as dextral strike-slip faults in the southern part of the Koralm Complex (Ottnangian to Karpatian: approximately 18–17 Ma) (Fig. 11a). In domains characterised by overlapping fault segments this was associated with
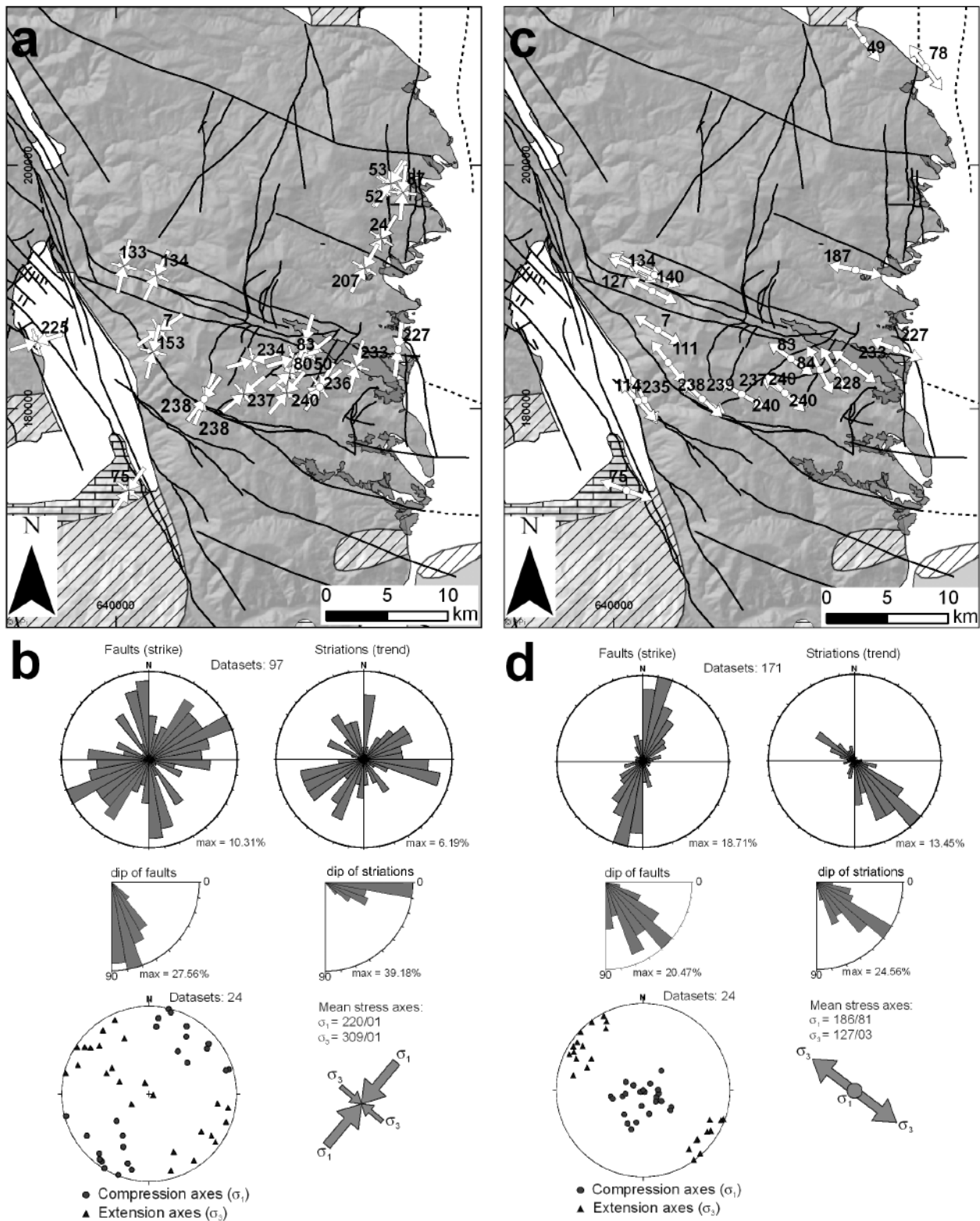
Fig. 8. a) Orientation of σ_1 (large arrows) and σ_3 (small arrows) related to D_{3-1}; Labeled numbers refer to Table 1. b) Rose diagrams with strike and dip of fault planes and trend of striations; orientation of σ_1 (filled circles) and σ_3 (triangles) of D_{3-1}-related tensors with mean maximum and minimum principal stress axes. c) Orientation of σ_1 (large arrows) and σ_3 (small arrows) related to D_{3-2}; labeled numbers refer to Table 1. d) Rose diagrams with strike and dip of fault planes and trend of striations; orientation of σ_1 (filled circles) and σ_3 (triangles) of D_{3-2}-related tensors with mean maximum and minimum principal stress axes. Refer to Figure 2 for legend of geological units. Grid is in Austrian BMN M34 system.
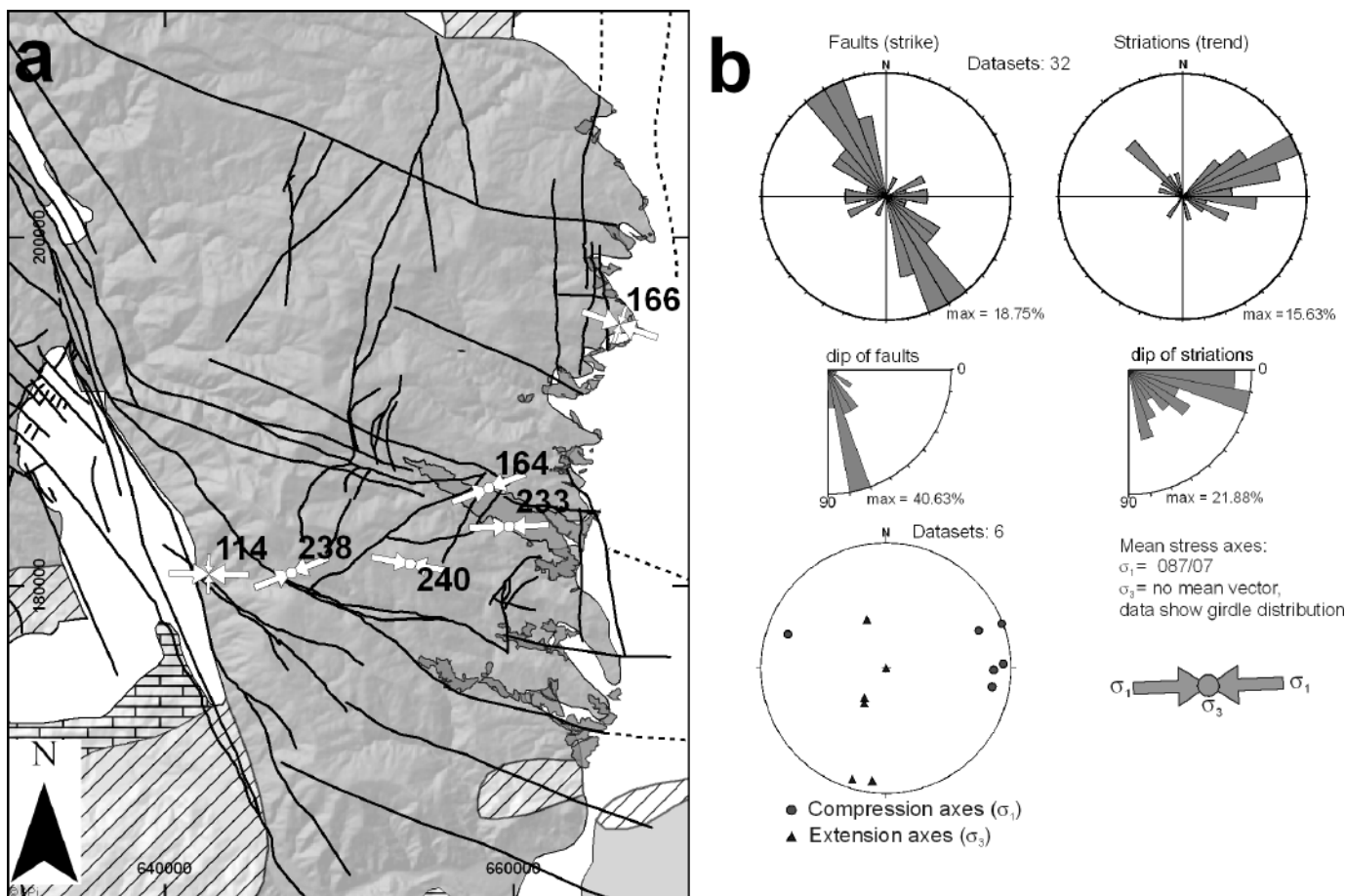
Fig. 9. a) Orientation of σ_1 (large arrows) and σ_3 (small arrows) related to D_4; labeled numbers refer to Table 1. b) Rose diagrams with strike and dip of fault planes and trend of striations; orientation of σ_1 (filled circles) and σ_3 (triangles) of D_4-related tensors with mean maximum and minimum principal stress axes. Refer to Figure 2 for legend of geological units. Grid is in Austrian BMN M34 system.

the evolution of WNW-trending troughs filled up with coarse block debris, e.g. the block debris of Schwanberg. This evolution continued with subsequent reactivation of E–W to WNW–ESE striking crustal fractures as normal faults, indicating (N)NE-(S)SW directed extension (D_{1-2}) (Fig. 11b). The lowermost parts of the block debris were partly crosscut by these high-angle normal faults, as locally observed within core drillings (Egger 2007), indicating partly synsedimentary faulting. The thickness of the deposits was acquired by both reflexion seismics and several drillings penetrating the contact between the block debris and the underlying basement. Sediment thickness amounts to approximately 180 meters in the central part, and decreases to 80 meters towards the margins of the basin. The base of the deposits was reached at an altitude of approximately 600 meters in the central parts, and approximately 700 meters close to the margins. Hence the base of the debris is situated 300 to 400 meters higher than the top of the western part of the Styrian Basin today (Egger 2007). The southern part of the Western Styrian Basin (Figs. 1, 2) was characterised by a fan-delta complex in a fault-controlled setting with 1000- to 2000 m thick coarse conglomerates close to the eastern margin of the Koralm Massif,

too (Ebner & Sachsenhofer 1995). It is assumed that this phase documents a first phase of considerable subsidence of the Styrian Basin in the time span from 18 to 16 Ma ago.

A similar tectonic evolution at a larger scale, with the development of an E-trending, fault-bounded trough (Ribnica-Selnica trough), may be observed along the northern margin of the Pohorje Massif (Figs. 1, 2, 11b) (Sachsenhofer et al. 1998; Vrabec & Fodor 2005) (Figs. 1, 2). Trough subsidence coincided with the exhumation of the Pohorje pluton showing a Miocene intrusion age (Fodor et al. 2008, this volume). During Middle Miocene time the Pohorje was already supplying sediment into the surrounding basins with nearly syn-sedimentary apatite cooling ages (Sachsenhofer at al. 1998; Dunkl et al. 2005). This phase of tectonic denudation by N–S-directed extension may therefore coincide with the climax of subsidence of the Styrian Basin during latest Karpatian times (approximately 17 Ma) (Sachsenhofer et al. 1997). The NNW-trending segments of the Lavanttal fault system were activated by dextral displacement (Fig. 11a), resulting in the formation of the Lavanttal Basin in a pull-apart manner (D_{1-1}) with subsequent subsidence due to NE–SW extension (D_{1-2}) (Fig. 11b).
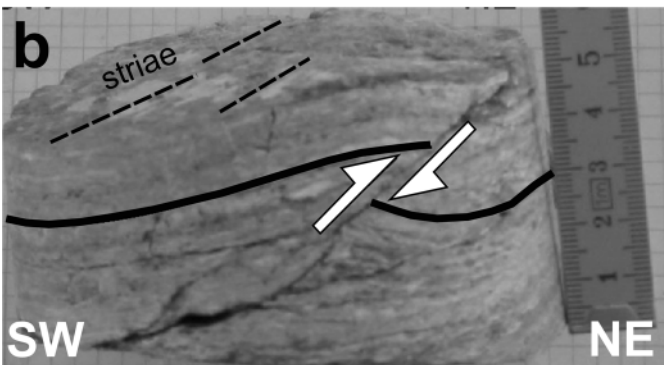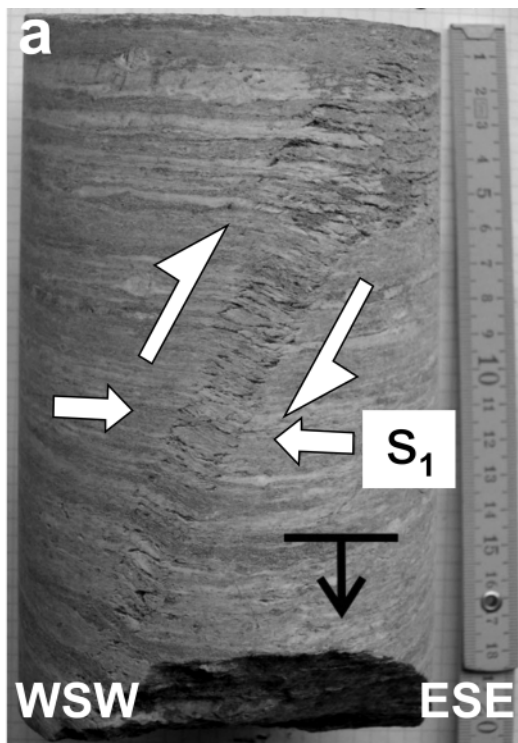
Fig. 10. D_4-related structures: kinkband (a) and s-type flanking folds with normal drag of foliation (b), both indicating top-to-the E reverse sense of shear; a) from drilling TB-D01/05, depth 303,8 m, specimen is 20 cm long; b) from drilling TB-D01/05, depth 291,9 m, vertical length of specimen is 6 cm.

E–W-directed extension (D_2) during the Badenian (approx. 16–13 Ma) resulted in the disintegration of the Styrian Basin into distinct sub-basins, separated by uplifted areas. This was mainly related to tilting of crustal blocks that coincided with the uplift of the Sausal Mountains (Figs. 1, 2), representing the so-called Middle Styrian Swell, and resulted in the separation of the western from the eastern Styrian Basin (Fig. 11c). The Western Styrian Basin is characterised by a lagoonal environment with siliciclastic sediments (Ebner & Sachsenhofer 1995), also along the previously formed E–W-trending troughs, and shows coarse grained alluvial and coastal deposits during this age. This phase of extension may also coincide with normal faulting along the eastern margin of the Koralm Massif, and

mainly oblique normal displacement along the Lavanttal fault. Related uplift of the Koralm Massif resulted in the separation of the Lavanttal Basin from the Styrian Basin.

Along the northern margin of the central Eastern Alps, this time span is characterised by the formation of pull apart basins along the Mur-Mürz fault system, in particular the Fohnsdorf Basin (e.g. Sachsenhofer et al. 2000; Strauss et al. 2001) and the Trofaiach Basin (e.g. Nievoll 1985) (Figs. 1, 2). These show a structural evolution that is quite similar to that of the southern part of the Koralm Massif – Styrian Basin system described so far. However, the well documented sedimentary evolution of the Fohnsdorf basin provides additional time constraints on the tectonic evolution of this area. Subsidence occurred along ENE-trending sinistral strike-slip faults and NE–SW to N–S trending normal faults during the Late Karpatian/Early Badenian, followed by N–S extension and normal faulting along the southern basin margin during the Middle/Late Badenian, altogether from approximately 17.2 to 15 Ma. Simultaneous dextral displacement and subsidence along the Lavanttal fault system allowed temporary marine influx from the Lavanttal basin towards north during the Early Badenian (Strauss et al. 2001). Post-Middle Badenian NNW–SSE directed shortening resulted in inversion of the Fohnsdorf Basin.

A sea level low stand at the Badenian/Sarmatian boundary caused erosional unconformities in parts of the Eastern Styrian Basin and the progradation of fluvial and deltaic sequences toward east (Ebner & Sachsenhofer 1995). The early Sarmatian (approximately 13 Ma) is marked by a transgressional phase, with deposition of shallow marine sediments. Northward propagation of sedimentation occurred mainly along N-trending fault zones. In the Western Styrian Basin Sarmatian sediments have only been observed in its northwesternmost parts (Flügel & Neubauer 1984). The lack of equivalent sediments in the rest of the Western Styrian Basin may result from erosion linked to Post-Sarmatian uplift. This is in accordance with the view of Dunkl et al. (2005) that the Eastern Alps between the Tauern Window and the Pannonian basin were covered by sediments more widely during the Early-Middle Miocene than recorded by the sediments still preserved today. Pannonian (11,5 to 7,1 Ma) sediments are restricted to the Eastern Styrian Basin and grade from fine-grained marine sands and marl to coarse grained siliciclastics related to alluvial fans during the early Pannonian (Ebner & Sachsenhofer 1995). A similar evolution can be observed in the Lavanttal Basin as well (e.g. Weber & Weiss 1983). This was associated with local inversion of E-trending troughs and the re-activation of E-trending and NNW-trending faults by sinistral and dextral displacement, respectively, due to NE-directed compression (D_{3-1}). Subsequent (S)SE-(N)NW-directed extension (D_{3-2}) caused the reactivation of N-trending normal faults along the eastern margin of the Koralm Massif and the Middle Styrian Swell, and of the Lavanttal fault by dextral normal oblique displacement (Fig. 11d).

During the Late Pannonian to Pliocene the entire Styrian Basin became an erosional domain, interpreted to coincide
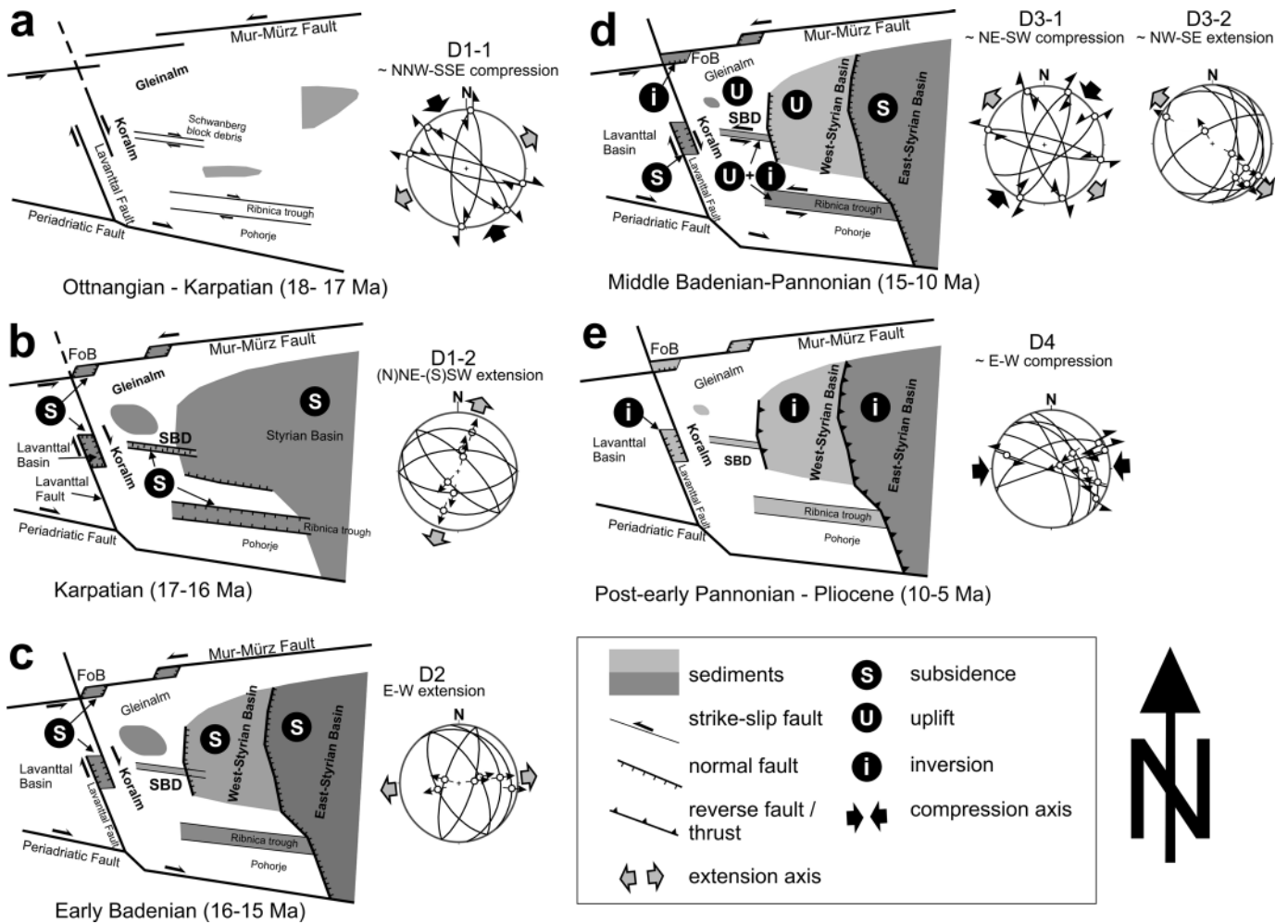
Fig. 11. Scheme of the tectonic evolution of the central southern Koralm Massif and the adjacent Styrian Basin during the Miocene. (FoB = Fohnsdorf Basin; SBD = Schwanberg block debris. Sketch is not to scale).

with a phase of basin inversion (D$_4$) (Fig. 11e). This phase can be related to the inversion of low-angle normal faults along the eastern margin of the Koralm Massif, related to E–W-directed compression being indicated by a sub-horizontal E–W-orientation of the maximum principal paleostress axes, resulting in the inversion of the Styrian and the Lavanttal Basins. Previously formed E–W striking structures probably were reactivated as tear faults, showing either dextral or sinistral displacement.

This structural succession, constrained by the sedimentary evolution of adjacent basins, indicates that the Koralm basement and the Western Styrian Basin were affected by post-Sarmatian uplift with respect to the Eastern Styrian Basin. For the timing of uplift this opens two possible interpretations:

(1) Uplift was mainly related to tilting of crustal blocks along east-directed normal or oblique normal faults, and contemporaneous to basin subsidence (compare Dunkl et al. 2005). This resulted in uplift of the Koralm Massif, including the block debris deposits of Schwanberg and Miocene deposits in the

northern part of the Koralm Massif, above the top of the Western Styrian Basin (Fig. 11d). The main final uplift of the Koralm Complex, partly together with the Western Styrian Basin, occurred during the Sarmatian.

(2) Uplift was related to W-directed inversion during the Pannonian and resulted in erosion of Sarmatian sediments in the western Styrian basin. However, as inversion affected the Styrian basin entirely it seems not to be a plausible mechanism for explaining the separation of the Styrian Basin into domains of distinct subsidence. Therefore, a model of extension-related uplift during the Sarmatian, according to (1), is favoured.

Irrespective of the mode of uplift the Koralm Complex was elevated by a minimum amount of approximately 800 m during this phase. Clastics previously deposited on top of the Koralm basement are at an altitude of ±1100 m today, in contrast to the top of the Styrian Basin, having an average altitude of ±300 m. This was accompanied by the development of a pronounced relief resulting in enhanced erosion and subsequent deposition of coarse-grained clastics in the Lavanttal and Eastern Styr-
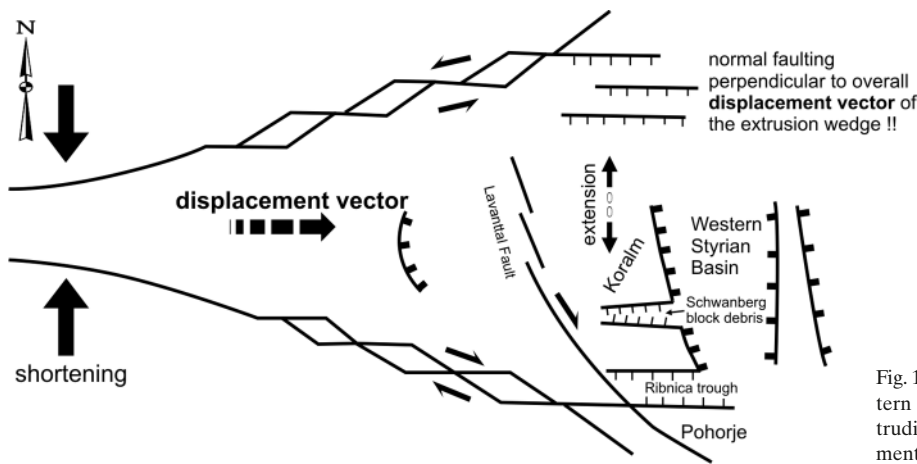
Fig. 12. Scheme showing the development of the fault pattern and related structures within an orogen-parallel extruding wedge, widening toward the direction of displacement. Sketch is not to scale.

ian Basin (Ebner & Sachsenhofer 1995; Reischenbacher et al. 2007).

The formation of the main fault sets in the area of investigation also reflects the structural evolution of an eastward extruding block with increasing width away from the central part of the Eastern Alpine orogen during orogen-parallel escape (e.g. Ratschbacher et al. 1989, 1991; Neubauer et al. 2000) (Fig. 12). This evolution is mainly governed by the northward indentation of a rigid indenter represented by the Southalpine (Fig. 1) accompanied with maximum shortening in the central Eastern Alps, and a continuous decrease of shortening toward east. According to Kuhlemann et al. (2003) this deformation episode occurred between 21 and 12 Ma. In the eastern part of the Eastern Alps, this extruding block is mainly characterised by strike-slip faulting along confining E–W-trending wrench faults associated with the formation of pull-apart basins at oversteps of distinct strike-slip faults, linked by approximately N-trending normal faults accommodating displacement along the mainly E-trending strike-slip fault zones (Fig. 12). These extensional structures form mainly perpendicular to the displacement vector. The eastward increasing width of the extruding wedge implies that progressive lateral displacement causes N–S-directed extension perpendicular to the overall displacement direction; this may be reflected in the re-activation of previously formed E-trending strike-slip faults and by the formation of additional E-trending extensional structures (Fig. 12).

The D_1–D_3 paleostress orientation patterns indicate an apparent clockwise rotation of the minimum principal stress (σ_3) from a N–S to a NW–SE orientation (Figs. 11a-d). However, this may just be related to counter clockwise rotation of crustal blocks, especially north of the Periadriatic fault, and is in accordance with paleomagnetic data indicating counter clockwise block rotation in the eastern part of the Eastern Alps by 30° to 40° in Middle Miocene times (approximately 17–13 Ma) (Fodor et al. 1998; Márton et al. 2000, 2002; Kuhlemann et al. 2003). Consequently, the apparent rotation of the regional stress field just results from passive rotation of the evaluated stress tensors. The subsequent inversion of the regional stress field to

E–W oriented compression (Fig. 11e) was described all over the eastern part of the Eastern Alps and the Pannonian Basin (Peresson & Decker 1997) and is interpreted to represent the far-field response of a phase of "soft continental collision" in the Eastern Carpathians. According to Peresson & Decker (1997), deformed Pannonian strata in the eastern Styrian Basin indicate that this paleostress regime may have started at 9 Ma and lasted approximately until 6 Ma.

6 Conclusions

1) The structural evolution of the Koralm Massif during the Neogene is determined by the development of two main fault sets: (a) E- to ESE-trending faults may have formed as strike slip faults with dextral sense of shear, linked by (b) approximately N-trending normal faults. Fault-related E-trending troughs were mainly filled up with block debris ("Schwanberger Blockschutt"); sedimentary deposits up to the Early/Middle Badenian are mainly related to E–W-striking faults.

2) During (N)NW-(S)SE-directed compression the E-trending structures were reactivated as high-angle normal faults or oblique normal faults, indicating a phase of (N)NE-(S)SW extension.

3) Main uplift of the Koralm Massif did not occur before the late Middle Miocene (Sarmatian).

4) Pannonian sedimentation was restricted to the Eastern Styrian Basin; this suggests uplift of the Western Styrian Basin together with the Koralm Complex and the block debris deposits at post-Sarmatian times; this is mainly related to displacement along E-dipping low-angle normal faults during a phase of E–W- to SE–NW-directed extension. The Koralm Complex was elevated by approximately 800 meters during this phase.

5) E–W directed contraction resulted in the reactivation of former low-angle normal faults as W-directed reverse faults, and the re-activation of E-trending structures as related tear faults; this coincides with the inversion of the Styrian Basin.

Acknowledgements

REFERENCES

Angelier, J. 1979. Determination of the mean principal direction of stresses for a given fault population. Tectonophysics 56, T17–T26.

Angelier, J. 1994: Fault slip analysis and paleostress reconstruction. In: Continental Deformation (Ed. by Hancock, P.L.). Pergamon Press, 53–100.

Angelier, J. & Mechler, P. 1977. Sur une méthode graphique de recherche des contraintes principales également utilisable en tectonique et en séismologie: la méthode des dièdres droits. Bulletin de la Société géologique France 19, 1309–1318.

Balogh, K., Ebner, F. and Ravasz, C. 1994. K/Ar-Alter tertiärer Vulkanite der südöstlichen Steiermark und des südlichen Burgenlands. In: Lobitzer, H. et al. (Eds.): Jubiläumsschrift 20 Jahre geologische Zusammenarbeit Österreich-Ungarn, Vol.2. Geologische Bundesanstalt, Wien, 55–72.

Beck-Mannagetta, P. 1952. Zur Geologie und Paläontologie des Tertiärs des unteren Lavanttales. Jahrbuch der Geologischen Bundesanstalt 95, 1–102

Beck-Mannagetta, P., Eisenhut, M., Ertl, V. and Homann, O., 1991. Geologische Karte der Republik Österreich 1:50.000–189 Deutschlandsberg. Geologische Bundesanstalt, Wien.

Bojar, H.-P., Bojar, A.-V., Mogessie, A., Fritz, H. & Thalhammer, O.A.R. 2001. Evolution of veins and sub-economic ore at Strassegg, Paleozoic of Graz, Eastern Alps, Austria: evidence for local fluid transport during metamorphism. Chemical Geology 175, 757–777.

Brodie, K., Fettes, D., Harte, B. & Schmid, R. 2002. Structural terms including fault rock terms. IUGS Subcommission on the Systematics of Metamorphic Rocks, 8 pp.

Brosch, F.J., Pischinger, G., Steidl, A., Vanek, R., & Decker, K. 2001: Improved site investigation results by kinematic discontinuity analysis on drill cores. In: Rock Mechanics – a Challenge for Society (Ed. by Särkkä & Eloranta). Swets & Zeitlinger Lisse, 41–45.

Caine, J.S., Evans, J.P. & Forster, C.B. 1996. Fault zone architecture and permeability structure. Geology 24, 1025–1028.

Chester, F.M. & Logan, J.M. 1986. Implications for mechanical properties of brittle faults from observations of the Punchbowl Fault, California. Pure and Applied Geophysics 124, 79–106.

Decker, K. & Peresson, H. 1996: Tertiary kinematics in the Alpine-Carpathian-Pannonian system: links between thrusting, transform faulting and crustal extension. In: Oil and Gas in Alpidic Thrustbelts and Basins of Central and Eastern Europe (Ed. by Wessely, G. & Liebl, W.). EAGE Special Publication, 69–77.

Doblas, M. 1998. Slickenside kinematic indicators. Tectonophysics 295, 187–197.

Dunkl, I., Kuhlemann, J., Reinecker, J. & Frisch, W. 2005. Cenozoic relief evolution of the Eastern Alps – Constraints from apatite fission track age-provenance of Neogene intramontane sediments. Austrian Journal of Earth Sciences (Mitteilungen der Österreichischen Geologischen Gesellschaft) 98, 92–105.

Ebner, F. & Sachsenhofer, R.F. 1995. Paleogeography, subsidence and thermal history of the Neogene Styrian Basin (Pannonian Basin system, Austria). Tectonophysics 242, 133–150.

Egger, M. 2007. Strukturelle Analyse des Schwanberger Blockschutt Beckens im Hinblick auf die Achse des Koralm-Basistunnels. Magisterarbeit, Institut für Angewandte Geowissenschaften, Technische Universität Graz, 66 pp.

Flügel, H.W. and Neubauer, F. 1984. Steiermark – Erläuterungen zur Geologischen Karte der Steiermark 1:200.000. Geologie der Österreichischen Bundesländer in kurzgefassten Einzeldarstellungen. Geologische Bundesanstalt, Wien, 127 pp.

Fodor, L., Jelen, B., Márton, E., Skaberne, D., Car, J. & Vrabec, M. 1998. Mio-Pliocene tectonic evolution of the Slovenian Periadriatic fault: Implications for Alpine-Carpathian extrusion models. Tectonics 17, 690–607.

Fodor, L. & POSIHU Research Group 2003. Miocene exhumation of the Pohorje-Kozjak Mts., Slovenia (Alpine-Pannonian transition). Geophysical Research Abstracts 5, 11814.

Fodor, L., Gerdes, A., Dunkl, I., Koroknai, B., Pécskay, Z., Trajanova, M., Horváth, P., Vrabec, M., Balogh, K., Jelen, B. & Frisch, W. 2008. Miocene emplacement and rapid cooling of the Pohorje pluton at the Alpine-Pannonian-Dinaric junction: a geochronological and structural study. Swiss Journal of Geosciences, doi: 10.1007/s00015-008-1286-9.

Frank, W. 1987: Evolution of the Austroalpine elements in the Cretaceous. In: Geodynamics of the Eastern Alps (ed. by Flügel, H.W. & Faupl, P.). Deuticke, 379–406.

Frisch, W., Dunkl, I. & Kuhlemann, J. 2000a. Post-collisional orogen-parallel large-scale extension in the Eastern Alps. Tectonophysics 327, 239–265.

Frisch, W., Kuhlemann, J., Dunkl, I. & Brügel, A. 1998. Palinspastic reconstruction and topographic evolution of the Eastern Alps during late Tertiary tectonic extrusion. Tectonophysics 297, 1–16.

Frisch, W., Szekely, B., Kuhlemann, J. & Dunkl, I. 2000b. Geomorphological evolution of the Eastern Alps in response to Miocene tectonics. Zeitschrift für Geomorphologie Neue Folge 44, 103–138.

Fritz, H., Krenn, K., Bojar, A.-V., Kurz, W., Hermann, S., Neubauer, F. & Robl, J. 2002. Late Cretaceous to Paleogene Tectonics and Metamorphism in the Eastern Alps: The "older" extrusion corridor. PANGEO Abstracts, 52–53.

Grasemann, B., Stüwe, K. & Vannay, J.-C. 2003. Sense and non-sense in flanking structures. Journal of Structural Geology 25, 19–34.

Habler, G. & Thöni, M. 2001. Preservation of Permo-Triassic low-pressure assemblages in the Cretaceous high-pressure metamorphic Saualpe crystalline basement (Eastern Alps, Austria). Journal of metamorphic Geology 19, 679–697.

Hejl, E. 1997. ‚Cold spots' during the Cenozoic evolution of the Eastern Alps: thermochronological interpretation of apatite fission-track data. Tectonophysics 272, 159–173.

Hejl, E. 1998. Über die känozoische Abkühlung und Denudation der Zentralalpen östlich der Hohen Tauern – eine Apatit-Spaltspurenanalyse. Mitteilungen der Österreichischen Geologischen Gesellschaft 89, 179–200.

Janák, M., Froitzheim, N., Vrabec, M., Krogh Ravna, E.J. & De Hoog, J.C.M. 2006. Ultrahigh-pressure metamorphism and exhumation of garnet peridotite in Pohorje, Eastern Alps. Jounal of metamorphic Geology 24, 19–31.

Kollmann, K., 1964. Jungtertiär im Steirischen Becken. Mitteilungen der Österreichischen Geologischen Gesellschaft, 57(2), 479–632.

Kuhlemann, J., Scholz, T. & Frisch, W. 2003. Postcollisional stress field changes in Eastern Carinthia (Austria). Mitteilungen der Österreichischen Geologischen Gesellschaft 94, 55–61.

Kurz, W. & Fritz, H. 2003. Tectonometamorphic evolution of the Austroalpine Nappe Complex in the central Eastern Alps – consequences for the Eo-Alpine evolution of the Eastern Alps. International Geology Review 45, 1100–1127.

Kurz, W., Fritz, H., Tenczer, V. & Unzog, W. 2002. Tectonometamorphic evolution of the Koralm Complex (Eastern Alps): Constraints from microstructures and textures of the "Plattengneis"-shear zone. Journal of Structural Geology 24, 1957–1970.

Linzer, H.-G., Decker, K., Peresson, H., Dell´Mour, R. & Frisch, W. 2002. Balancing lateral orogenic float of the Eastern Alps. Tectonophysics 354, 211–237.

Márton, E., Fodor, L., Jelen, B., Márton, P., Rifelj, H. & Kevric, R. 2002. Miocene to Quarternary deformation in NE Slovenia: complex paleomagnetic and structural study. Journal of Geodynamics 34, 627–651.

Márton, E., Kuhlemann, J., Frisch, W. & Dunkl, I. 2000. Miocene rotations in the Eastern Alps – paleomagnetic results from intramontane basin sediments. Tectonophysics 323, 163–182.

Marret, R. and Allmendinger, R.W., 1990. Kinematic analysis of fault-slip data. Journal of Structural Geology 12, 973–986.

Medley, E.W. 1994. The Engineering Characterization of Melanges and Similar Block-in-Matrix Rocks (Bimrocks). Ph.D. dissertation, University of California at Berkley, 175 pp.

Meschede, M. 1994. Methoden der Strukturgeologie. Ferdinand Enke Verlag Stuttgart, 169 pp.

Meschede, M. and Decker, K. 1993. Störungsflächenanalyse entlang des Nordrandes der Ostalpen – ein methodischer Vergleich. Zeitschrift der Deutschen geologischen Gesellschaft, 144(2), 419–433.

Nebert, K., 1989. Das Neogen zwischen Sulm und Lassnitz (Suedweststeiermark). Jahrbuch der Geologischen Bundesanstalt 132, 727–743.

Neubauer, F., Dallmeyer, R.D., Dunkl, I. & Schirnik, D. 1995. Late Cretaceous exhumation of the metamorphic Gleinalm dome, Eastern Alps: kinematics, cooling history and sedimentary response in a sinistral wrench corridor. Tectonophysics 242, 79–98.

Neubauer, F., Fritz, H., Genser, J., Kurz, W., Nemes, F., Wallbrecher, E., Wang, X., & Willingshofer, E. 2000: Structural evolution within an extruding wedge: model and application to the Alpine-Pannonian system. In: Aspects of Tectonic Faulting (Ed. by Lehner, F.K. & Urai, J.L.). Springer, 141–153.

Neubauer, F. & Genser, J. 1990. Architektur und Kinematik der östlichen Zentralalpen – eine Übersicht. Mitteilungen des naturwissenschaftlichen Vereins für Steiermark 120, 203–219.

Nievoll, J. 1985. Die brruchhafte Tektonik entlang der Trofaiachlinie (Östliche Zentralalpen, Österreich). Jahrbuch der Geologischen Bundesanstalt 127, 643–671.

Ortner, H., Reiter, F. and Acs, P. 2002. Easy handling of tectonic data: the programs TectonicVB for Mac and TectonicsFP for Windows(TM). Computers & Geosciences, 28(10), 1193–1200.

Peresson, H. & Decker, K. 1997. Far-field effects of Late Miocene subduction in the Eastern Carpathians: E–W compression and inversion of structures in the Alpine-Carpathian-Pannonian region. Tectonics 16, 38–56.

Petit, J.P. 1987. Criteria for the sense of movement on fault surfaces in brittle rocks. Journal of Structural Geology 9, 597–608.

Piller, W.E. & 18 co-authors 2004. Die Stratigraphische Tabelle von Österreich 2004 (sedimentäre Schichtfolgen). Österreichische stratigraphische Kommission und Kommission für die paläontologische und stratigraphische Erforschung Österreichs der Österreichischen Akademie der Wissenschaften.

Piller, W.E., Harzhauser, M. & Mandic, O. 2007. Miocene Central Paratethys stratigraphy – current status and future directions. Stratigraphy 4, 151–168.

Pischinger, G., Brosch, F.J., Fasching, A., Fuchs, R., Goricki, A., Müller, H., Otto, R., Steidl, A. & Vanek, R. 2005. Brittle faulting in the Koralm region – results from the site investigation for the Koralmtunnel. Abstract, Symposium Geologie AlpTransit, Zürich.

Pischinger, G., Brosch, F.-J., Kurz, W. & Rantisch, G. 2006. Normal faulting in a rigid basin boundary block – field evidence from the Koralm Complex (Eastern Alps). Innsbruck University Press Conference Series, PANGEO Austria 2006, 250–251.

Puch, T. 1995: Spaltspurendatierungen an Apatit und Zirkon als Tracer tektonischer Prozesse im Bereich Koralpe-Saualpe-Krappfeld (Kärnten/ Österreich), Ostalpen. Unveröff. Diplomarbeit, Naturwissenschaftliche Fakultät, Universität Graz, 124 pp.

Rabitsch, R., Wölfler, A. & Kurz, W. 2007. Fission track dating in fault zones: an example from the Eastern Alps. Geophysical Research Abstracts 9, EGU2007-A-02732.

Ratschbacher, L., Frisch, W., Linzer, H.-G. & Merle, O. 1991. Lateral Extrusion in the Eastern Alps. Part 2: Structural Analyses. Tectonics 10/2, 257–271.

Ratschbacher, L., Frisch, W., Neubauer, F., Schmid, S.M. & Neugebauer, J. 1989. Extension in compressional orogenic belts: The eastern Alps. Geology 17, 404–407.

Reinecker, J. 2000. Stress and deformation: Miocene to present-day tectonics in the Eastern Alps. Tübinger Geowissenschaftliche Arbeiten Serie A 55, 128 pp.

Reinecker, J. & Lenhardt, W.A. 1999. Present-day stress field and deformation in eastern Austria. International Journal of Earth Sciences 88, 532–550.

Reischenbacher, D., Rifelj, H., Sachsenhofer, R., Jelen, B., Coric, S., Gross, M. & Reichenbacher, B. 2007. Early Badenian paleoenvironment in the Lavanttal Basin (Mühldorf Formation; Austria): Evience from geochemistry and paleontology. Austrian Journal of Earth Sciences 100, 202–229.

Reiter, F. & Acs, P. 1996–2001. Tectonics FP 1.6.2, a 32-bit Windows™-Software for Structural Geology.

Sachsenhofer, R.F. 1996. The Neogene Styrian Basin: An Overview. Mitteilungen der Gesellschaft der Geologie und Bergbaustudenten in Österreich 41, 19–32.

Sachsenhofer, R.F., Dunkl, I., Hasenhüttl, C. & Jelen, B. 1998. Miocene thermal history of the southwestern margin of the Styrian Basin: vitrinite reflectance and fission-track data from the Pohorje/Kozjak area (Slovenia). Tectonophysics 297, 17–29.

Sachsenhofer, R.F., Jelen, B., Hasenhüttl, C., Dunkl, I. & Rainer, T. 2001. Thermal history of Tertiary basins in Slovenia (Alpine-Dinaride-Pannonian junction). Tectonophysics 334, 77–99.

Sachsenhofer, R.F., Lankreijer, A., Cloething, S. & Ebner, F. 1997. Subsidence analysis and quantitative basin modelling in the Styrian Basin (Pannonian Basin System, Austria). Tectonophysics 272, 175–196.

Sachsenhofer, R.F., Kogler, A., Polesny, H., Strauss, P. & Wagreich, M. 2000. The Neogene Fohnsdorf Basin: basin formation and basin inversion during lateral extrusion in the Eastern Alps (Austria). International Journal of Earth Sciences 89, 415–430.

Schmid, S.M., Fügenschuh, B., Kissling, E. and Schuster, R., 2004. Tectonic map and overtall architecture of the Alpine orogen. Eclogae geologicae Helvetiae 97, 93–117.

Schuster, R. & Kurz, W. 2005. Eclogites in the Eastern Alps: High-pressure metamorphism in the context of Alpine orogeny. Mitteilungen der Österreichischen Mineralogischen Gesellschaft 150, 183–198.

Spang, J.H. 1972. Numerical Method for Dynamic Analysis of Calcite Twin Lamellae. Geological Society of America Bulletin, 83(2), 467–471.

Steidl, A., Goricki, A., Schubert, W. & Riedmüller, G. 2001. Geological and Geotechnical Ground Characterisation for the Koralm Tunnel Route Selection. Felsbau 19, 14–21.

Stiny, J. 1925. Gesteinsklüftung im Teigitschgebiet. Tschermaks Mineralogische und Petrographische Mitteilungen 38, 464–478.

Strauss, P., Wagreich, M., Decker, K. & Sachsenhofer, R.F. 2001. Tectonics and sedimentation in the Fohnsdorf-Seckau Basin (Miocene, Austria): from a pull-apart basin to a half-graben. International Journal of Earth Sciences 90, 549–559.

Turner, F.J. 1953. Nature and dynamic interpretation of deformation lamellae in calcite of three marbles. American Journal of Science 251, 276–298.

Vanek, R., Pischinger, G. & Brosch, F.J. 2001. Kinematic discontinuity analysis – results and implications of structural geological investigations on drill cores. Felsbau 19, 31–36.

Vrabec, M. & Fodor, L. 2005: Late Cenozoic tectonics of Slovenia: Structural styles at the northeastern corner of the Adriatic microplate. In: The Adriatic Microplate: GPS, Geodesy, Tectonics and Hazards (Ed. by Pinter, N., Grenerczy, J., Weber, D., Medak, D., & Stein, S.). Kluwer Academic Publishers, 1–18.

Wallbrecher, E. (1986): Tektonische und gefügeanalytische Arbeitsweisen. – Enke-Verlag, Stuttgart, 244 pp.

Weber, L. & Weiss, A. 1983. Bergbaugeschichte und Geologie der Österreichischen Braunkohlevorkommen. Archiv für Lagerstättenforschung der Geologischen Bundesanstalt 4, 1–317.